THE STRUCTURES OF TITANIA NANOTUBE ARRAYS SYNTHESIZED BY ONE-FACED ANODIZATION

THANAPORN THUMSA-ARD

A THESIS SUBMITTED IN PARTIAL FULFILLMENT OF THE
REQUIREMENTS FOR THE DEGREE
OF DOCTOR OF PHILOSOPHY
MAJOR IN PHYSICS
FACULTY OF SCIENCE
UBON RATCHATHANI UNIVERSITY
ACADEMIC YEAR 2018

ACKNOWLEDGEMENTS

This work would not have been possible without the financial support from Science Achievement Scholarship of Thailand (SAST). Firstly, I would like to express my sincere gratitude to my advisors Asst. Prof. Dr. Udom Tipparach and Dr. Orathai Thumthan for the continuous support of my Ph.D study and related research, for his patience, motivation, and immense knowledge. Their guidance helped me in all the time of research and writing of this thesis. I could not have imagined having a better advisor and mentor for my Ph.D study.

Besides my advisors, I would like to thank the rest of my thesis committee: Assoc. Prof. Dr. Tosawat Setawan and Asst. prof. Dr. Tanin Nutaro for their insightful comments and encouragement, but also for the hard question which incented me to widen my research from various perspectives.

My sincere thanks also goes to Dr. Ongard Thiabgoh, who guided me about the technique of English research writing, Mr. Narongsak Kodtharin, who helped me to conduct anodization method and Mr. Wichean Piwbang, who provided me about how to characterize XRD technique. Without they precious support it would not be possible to conduct this research.

Thanaporn Thumsa-ard
Researcher

บทคัดย่อ

เรื่อง : โครงสร้างของท่อนาโนไททาเนียที่ถูกสังเคราะห์โดยวิธีการแอโนไดเซชันแบบด้านเดียว
ผู้วิจัย : ธนาภรณ์ ทำสะอาด
ชื่อปริญญา : ปรัชญาดุษฎีบัณฑิต
สาขาวิชา : ฟิสิกส์
อาจารย์ที่ปรึกษาหลัก : ผู้ช่วยศาสตราจารย์ ดร.อุดม ทิพราช
อาจารย์ที่ปรึกษาร่วม : ดร.อรทัย ทุมทัน
คำสำคัญ : ไททาเนีย, การแอโนไดเซชัน, ไททาเนียมไดออกไซด์, ท่อนาโน, โพแตสเซียมเฟอริไซยาไนด์

ท่อนาโนไททาเนีย (TiO_2) ที่มีการจัดเรียงตัวกันอย่างเป็นระเบียบถูกสังเคราะห์ขึ้นโดยวิธีการแอโนไดเซชันแบบด้านเดียว แผ่นไททาเนียมถูกแอโนไดในเอทิลีนไกลคอลซึ่งเป็นสารละลายอิเล็กโทรไลต์ที่ประกอบไปด้วยแอมโมเนียมฟลูออไรด์ 0.25 wt% น้ำที่ปราศจากไอออน 2 vol% และเจือด้วยโพแตสเซียมเฟอริไซยาไนด์ที่ความเข้มข้นต่างๆ โดยให้ศักย์ไฟฟ้า 50 โวลต์เป็นเวลา 2 ชั่วโมงที่อุณหภูมิห้อง ตัวอย่างที่ถูกแอโนไดถูกนำไปบำบัดด้วยความร้อนที่ 450 องศาเซลเซียส เป็นเวลา 2 ชั่วโมงเพื่อเปลี่ยนไททาเนียแบบอสัณฐานเป็นอะนาเทสผลึกนาโน ท่อนาโนไททาเนียที่มีการจัดเรียงตัวกันอย่างเป็นระเบียบสามารถสังเคราะห์ขึ้นได้หลังจากโพแตสเซียมเฟอริไซยาไนด์ที่ความเข้มข้นต่างๆถูกเจือ พื้นผิวของท่อนาโนไททาเนียมไดออกไซด์เรียบขึ้นหลังจากความเข้มข้นของโพแตสเซียมเฟอริไซยาไนด์เพิ่มขึ้น ยืนยันโดยการวัดด้วยเทคนิค AFM การดูดกลืนสเปกตรัมแสงของตัวอย่างถูกขยายในช่วง 200 ถึง 375 นาโนเมตร และค่าแถบช่องว่างพลังงานของตัวอย่างเพิ่มขึ้นเล็กน้อยเมื่อโพแตสเซียมเฟอริไซยาไนด์ถูกเจือ การเจือโพแตสเซียมเฟอริไซยาไนด์ที่ความเข้มข้น 0.20 wt% เป็นผลให้ Ti 2p เลื่อนไปยังพลังงานยึดเหนี่ยวที่ต่ำกว่า เนื่องจากการลดลงของ Ti^{4+} เป็น Ti^{3+} ซึ่งนำไปสู่การปรับปรุงประสิทธิภาพทางไฟฟ้าเคมีของท่อนาโนไททาเนีย ตัวอย่างท่อนาโนไททาเนียที่ถูกเจือด้วยโพแตสเซียมเฟอริไซยาไนด์ที่ความเข้มข้น 0.20 wt% ถูกนำไปใช้เป็นโฟโตแอโนดในเซลล์แสงอาทิตย์ชนิดสีย้อมไวแสง และให้ประสิทธิภาพสูงที่สุดเมื่อเทียบกับตัวอย่างอื่นๆ งานวิจัยนี้ได้เสนอแนะวิธีการทางเลือกเพื่อการสังเคราะห์ท่อนาโนไททาเนียมไดออกไซด์ที่สามารถใช้เป็นวัสดุผันพลังงาน

ABSTRACT

TITLE : THE STRUCTURES OF TITANIA NANOTUBE ARRAYS SYNTHESIZED BY ONE-FACED ANODIZATION
AUTHOR : THANAPORN THUMSA-ARD
DEGREE : DOCTOR OF PHILOSOPHY
MAJOR : PHYSICS
ADVISOR : ASST. PROF. UDOM TIPPARACH, Ph.D.
CO-ADVISOR : ORATHAI THUMTHAN, Ph.D.
KEYWORDS : TITANIA, ANODIZATION, TITANIUM DIOXIDE, NANOTUBES, POTASSIUM FERRICYANIDE

Highly ordered titania (TiO_2) nanotube arrays were synthesized via one-faced and single-step anodization method. Titanium foils were anodized in ethylene glycol based electrolytes containing 0.25 wt% NH_4F, 2 vol% H_2O, and doped with various concentrations of $K_3[Fe(CN)_6]$ at applied voltage of 50 V for 2 h at room temperature. As-anodized samples were annealed at 450 °C for 2 h in order to transform the amorphous titania to nanocrystalline anatase. Highly ordered titania nanotube arrays were obtained after $K_3[Fe(CN)_6]$ at different concentrations was introduced. The surfaces of TiO_2 nanotubes were smoother after increasing concentrations of $K_3[Fe(CN)_6]$, confirmed by AFM investigation. The absorption spectra of the samples were extended in range of 200 to 375 nm and slightly increased in band gap energies of titania when $K_3[Fe(CN)_6]$ was doped. Doping with 0.20 wt% $K_3[Fe(CN)_6]$ caused Ti 2p shifted towards lower binding energy due to the reduction of Ti^{4+} to Ti^{3+} and led to improve the electrochemical performance of titania nanotubes. The 0.20 wt% $K_3[Fe(CN)_6]$ doped titania nanotube sample was used as photoanode in DSSC and exhibited highest solar cell efficiency than other samples. This work suggests an alternative method for fine tuning the size of TiO_2 nanotube arrays that can be used as energy conversion materials.

CONTENTS

CONTENTS (CONTINUED)

PAGE

CHAPTER 5 CONCLUSION AND RECOMMENDATION

LIST OF TABLES

LIST OF FIGURES

FIGURE **PAGE**

LIST OF FIGURES (CONTINUED)

LIST OF FIGURES (CONTINUED)

LIST OF FIGURES (CONTINUED)

FIGURE **PAGE**

LIST OF ABBREVIATIONS

ABBREVIATION	MEANING
GHG	Greenhouse gas
DSSCs	Dye-sensitized solar cells
XRD	X-ray diffraction
SEM	Scanning electron microscopy
AFM	Atomic force microscopy
XPS	X-ray photoelectron spectroscopy
EDS	Energy dispersive X-ray spectroscopy
PV	Photovoltaic
TCO	Transparent conducting oxide
PSC	Photoelectrochemical solar cells
LHE	Light-harvesting efficiency
QD	Quantum dot
e^-	Electron
s	Dye molecule
s^*	Excited dye molecule
s^+	dye molecule after release an electron
I^-	Iodide
I^-_3	Tri iodide
PSPD	Position sensitive photo-detector
UV/Vis	Ultraviolet Visible
MK	Kubelka-Munk
E_g	Band gap energy
A	Optical intensity
d	Thickness of the sample
υ	Frequency of incident light
β	Constant
h	Plank’s constant
UHV	Ultra-high vacuum

LIST OF ABBREVIATIONS (CONTINUED)

ABBREVIATION	**MEANING**
FF	Fill-factor
η	Conversion efficiency
V_{oc}	Open circuit voltage
I_{sc}	Short circuit current density
V_{mp}	Voltage at maximum power
I_{mp}	Current at maximum power
P_{in}	Incident light power
R_q	Root mean square roughness
$R_{p\text{-}v}$	Ratio of peak to valley
R_{ave}	Average roughness

CHAPTER 1

INTRODUCTION

This chapter provides the rational and background of the energy conversion material in type of dye-sensitized solar cell which is used for converting solar energy to electrical energy by using TiO_2 nanotubes as photoanodes. This chapter also mentions the research objectives, the scope of research, the research site, and expected outcomes.

1.1 Introduction and background

The increasing energy demand in the developing countries from fossil fuels plays a key role in the upward trend in greenhouse gas (GHG) emissions and air pollutants and can cause poverty, pollution, health and environmental problems. Solar energy is the best answer, an appropriate technology for a source of renewable electricity [1, 2]. Dye sensitized solar cells (DSSCs) are particularly attractive for a topic of significant research in the last two decades because of their fundamental and scientific importance in the area of energy conversion by alternative concept to present the p–n junction photovoltaic devices with high efficiency, low fabrication cost and easy preparation method. The efficiency of DSSCs could be reach approximately 11% which is low commercial application [3-7]. One of the ways to develop the DSSC efficiency is using of TiO_2 as photoanodes in DSSCs such as TiO_2 for the anode in dye sensitized solar cells cathode using recycled battery [8], TiO_2 nanostructues for dye-sensitized solar cell [9-11], unique TiO_2 paste for high efficiency dye-sensitized solar cells [12], TiO_2 by sol–gel blocking layers for dye-sensitized solar cells [13].

In recent decades, titanium dioxide nanostructures or titania (TiO_2) such as TiO_2 nanorods [14], TiO_2 nanobelts [15], TiO_2 nanowires [16], TiO_2 nanoparticles [17], TiO_2 nanoflowers [18], TiO_2/TiB_2 nanowalls [19], TiO_2 nanopowders [20], TiO_2 nanosheets [21], TiO_2 nanofibers [22], TiO_2 nanoribbons [23], TiO_2 nanospheres [24], TiO_2 nanodots [25], TiO_2 nanocubes [26], TiO_2 nanoclusters [27], TiO_2 nanocones [28], TiO_2 nanotubes [29], etc., have attracted much attention from scientists and engineers in various areas because of their wide applications in environment [30], photocatalytic [31], dye sensitized solar cell [32], air treatment [33], water splitting [34], and others. In general, titanium dioxide (TiO_2) has three phases including anatase, rutile and brookite. Anatase phase is exceptional in photocatalytic activity due to its high reflection index, low extinction coefficient, non-toxicity, high chemical and physical stability, and low cost [35]. There are a number of methods to fabricate TiO_2 nanostructures such as hydrothermal synthesis [36], chemical vapor deposition [37], atmospheric pressure plasma jet [38], electrospinning [39], atomic layer deposition [40], and others. Among these, anodization process of TiO_2 nanotubes is simple and inexpensive. Numerous experimental evidences suggest that TiO_2 nonotubes possess the exceptional properties: high electron transport, large electron diffusion length, and relative band-edge position which are suitable to trigger a wide range of photocatalytic reaction [41,42]. However, TiO_2 performance is relative low for the applications of photocatalysis due to its wide band gap energy of 3.0-3.2 eV. In order to enhance the performance of TiO_2, it must be improved by doping some elements, for example, Mg and Mg-Nb on TiO_2 [43], Cu on two-dimensional TiO_2 nanowalls [44], S on TiO_2 nanofibers [45], Fe, Ni, Co or Zn on TiO_2 nanoparticles [46], Na on TiO_2 nanorods [47], and CdTe on TiO_2 nanoarchitectures [48]. Previous research has been conducted to improve the performance of TiO_2. For example, the transition-metal-doped TiO_2 nanotubes are highly visible-active and stable, excellent photoelectrochemical properties, and photocatalytic activities under visible light irradiation [49, 50]. Further, The Fe^{3+} doped TiO_2 nanotubes synthesized by a solvothermal method in $FeCl_3$ solution indicate significant enhancement of the visible light absorption and exhibit excellent photocurrent and photoelectrochemical performance [51].

Here, this study contributes to the enhancement of TiO_2 nanotubes in dye-sensitized solar cell applications and presents the investigation of the effect of potassium ferricyanide ($K_3[Fe(CN)_6]$) on TiO_2 nanotubes. In photoelectrochemical solar cell applications, $K_3[Fe(CN)_6]$ is widely used as photoelectroactive electrolyte [52], because it comprises K, Fe, C, and N which have high potential for improvement on the performance of TiO_2 nanotubes.

In this work, highly ordered TiO_2 nanotubes were fabricated through one-faced and single-step anodization on titanium foils by varying amounts of $K_3[Fe(CN)_6]$ in ethylene glycol based electrolyte. The physical and chemical characteristics of as-prepared samples were investigated using X-ray diffraction (XRD), Scanning electron microscopy (SEM), Atomic force microscopy (AFM), X-ray photoelectron spectroscopy (XPS), Energy dispersive X-ray spectroscopy (EDS), and UV-Vis spectroscopy. Furthermore, the obtained samples were applied for DSSCs and their photo-conversion efficiencies were investigated and calculated by the current-voltage (I-V) characteristics.

1.2 Research objectives

1.2.1 To fabricate highly ordered TiO_2 nanotubes through one-faced and single-step anodization on titanium foils by varying amounts of $K_3[Fe(CN)_6]$ in ethylene glycol based electrolyte.

1.2.2 To characterize the physical and chemical characteristics of the samples using XRD, SEM, AFM, XPS, EDS, and UV- Vis spectroscopy.

1.2.3 To investigate and calculate the photoconversion efficiency of the photoanodes by the current-voltage (I-V) characteristics.

1.3 Scope of research

This research aims to synthesize highly ordered TiO_2 nanotubes through one-faced and single-step anodization on titanium foils by varying amounts of $K_3[Fe(CN)_6]$ in ethylene glycol based electrolyte and characterize the physical and chemical characteristics of the samples using XRD, SEM, AFM, XPS, EDS, and UV- Vis spectroscopy. The photo conversion efficiency of them would be obtained.

1.4 Research site

Department of Physics, Faculty of Science, Ubon Ratchathani University

1.5 Expected outcomes

1.5.1 Obtain high density and self-organized TiO_2 nanotubes.

1.5.2 Achieve anatase phase structures of the specimens in the XRD patterns.

1.5.3 Attain the nanostructures of synthesized products in SEM images.

1.5.4 Accomplish the photo conversion efficiency of the photoanodes.

CHAPTER 2

LITERATURE REVIEWS

This chapter deals with the theory and literature reviews which include the fundamental principal of dye-sensitized solar cells (DSSCs) concept, TiO_2 nanotube materials which used for photoanodes in DSSCs, anodization method for TiO_2 nanotube fabrication and some information on potassium ferricyanide dopant.

2.1 Dye-sensitized solar cells (DSSCs)

The technology of solar energy is a key important role in the field of sustainable energy or renewable energy, because it does not release air pollutant during generate power energy but reduces the emission of greenhouse gases. Solar energy is considered as a feasible alternative because “More energy from sunlight strikes on Earth in 1 hour than all of the energy consumed by humans in an entire year”[2]. A solar cell is a photonic device that converts photons with specific wavelengths to electricity [53]. After Alexandre Edmond Becquerel discovered the photoelectrochemical (photovoltaic) effect in 1839 while he was investigating the effect of light on metal electrodes immersed in electrolyte, research in this area continued and technology developed to produce many types and structures of the materials presently used in photovoltaic (PV) technology. First and second generations photovoltaic cells are mainly constructed from semiconductors including crystalline silicon, III-V compounds, cadmium telluride, and copper indium selenide/sulfide [54]. Low cost solar cells have been the subject of intensive research work for the last three decades. Amorphous semiconductors were announced as one of the most promising materials for low cost energy production. However, dye sensitized solar cells (DSSCs) emerged as a new class of low cost energy conversion devices with simple manufacturing procedures. General comparison between semiconductor-based solar cells and dye sensitized solar cells is presented in Table 2.1.

Incorporation of dye molecules in some wide band-gap semiconductor electrodes was a key factor in developing photoelecrochemical solar cells. Michael

Gratzel and coworkers at the Ecole Polytechnique Federale de Lausanne succeeded for the first time to produce what is known as “Gratzel Cell” or Dye sensitized solar cells (DSSCs) to imitate photosynthesis. The natural process, plants convert sunlight into energy by sensitizing a nanocrystalline TiO_2 film using novel Rubipyridl complex. In dye sensitized solar cells (DSSCs), charge separation is accomplished by kinetic competition similar in photosynthesis leading to photovoltaic action. It has been shown that DSSC are promising class of low cost and moderate efficiency solar cell as shown in table 2.2 based on organic materials [55].

Table 2.1 Comparison between semiconductor solar cells and the dye sensitized solar cells (DSSCs) [54].

	Semiconductor solar cells	**DSSC**
Transparency	Opaque	Transparent
Pro-Environment (Material and Process)	Normal	Great
Power generation cost	High	Low
Power generation efficiency	High	Normal
Color	Limited	Various

In fact, in semiconductor p-n junction solar cells, charge separation is taken care by the junction built in electric field, while in dye sensitizes solar cell charge separation is by kinetic competition as in photosynthesis [56]. The organic dye monolayer in the photoelectrochemical or dye sensitized solar cells replaces light absorbing pigments (chlorophylls), the wide band gap nanostructured semiconductor layer replaces oxidized dihydro-nicotinamide-adenine-dinucleotide phosphate (NADPH), and carbon dioxide acts as the electron acceptor. Moreover, the electrolyte replaces the water while oxygen as the electron donor and oxidation product, respectively [57]. The overall cell efficiency of dye sensitized solar cell is found to be proportional to the electron injection efficiency in the wide band gap nanostructured semiconductors. This finding has encouraged researchers over the past decades. ZnO_2

nanowires, for example, have been developed to replace both porous and TiO_2 nanoparticle based solar cells [58]. Also, metal complex and novel manmade sensitizers have been proposed.

Table 2.2 Confirmed terrestrial cell efficiencies measured under the global AM 1.5 spectrum (1000 W· m^{-2}) at 25 °C. (ap)=aperture area; (t)=total area; (da)=designated irradiance area. FhG-ISE=Fraunhofer-Institute for Solar Energy system; JQA = Japan Quality Assurance [54].

Classification	η (%)	Area (cm^2)	V_{oc} (V)	J_{sc} ($mA.cm^{-2}$)	FF
Silicon					
Si (crystalline)	24.7±0.5	4.00 (da)	0.706	42.2	0.83
Si (multicrystalline)	19.8±0.5	1.09 (ap)	0.654	38.1	0.08
Si (thin-film transfer)	16.6±0.4	4.02 (ap)	0.645	32.8	0.78
III-V cells					
GaAs (crystalline)	25.1±0.8	3.91(t)	1.022	28.2	0.87
GaAs (Thin film)	23.3±0.7	4.00(ap)	1.011	27.6	0.84
GaAs (multicrystalline)	18.2±0.5	4.01(t)	0.994	23.0	0.80
InP (crystalline)	21.9±0.7	4.02(t)	0.878	29.3	0.85
Polycrystalline thin film					
$CuInGaSe_2$ (CIGS)	18.4±0.5	1.04(t)	0.669	35.7	0.77
CdTe	16.5±0.5	1.13(ap)	0.845	26.7	0.76
Amorphous/ microcrystalline Si					
Si (nanocrystalline)	10.1±0.2	1.20(ap)	0.539	24.4	0.77
Photoelectrochemical cells					
Nanocrystalline dye	11.0±0.5	0.25(ap)	0.795	19.4	0.71
Nanocrystalline dye (submodule)	4.7±0.2	141.4(ap)	0.795	11.3	0.59

Table 2.2 Confirmed terrestrial cell efficiencies measured under the global AM 1.5 spectrum (1000 W· m^{-2}) at 25 °C. (ap)=aperture area; (t)=total area; (da)=designated irradiance area. FhG-ISE=Fraunhofer-Institute for Solar Energy system; JQA = Japan Quality Assurance (continued) [54].

Classification	**η (%)**	**Area (cm^2)**	**V_{oc} (V)**	**J_{sc} (mA.cm^{-2})**	**FF**
Multijunction cells					
GaInP/GaAs	30.3	4.0 (t)	2.488	14.22	0.86
GaInP/GaAs/Ge	28.7±1.4	29.93(t)	2.571	12.95	0.86
GaAs/CIS (thin film)	25.8±1.3	4.00 (t)	-	-	-
a-Si/CIGS (thin film)	14.6±0.7	2.40 (ap)	-	-	-

However, processing and synthesization of these sensitizers are complicated and costly processes. Development or extraction of photosensitizers with absorption range extended to the near IR is greatly desired.

The sintered mesoporous titanium dioxide (TiO_2) was used and developed to establish DSSC technology. That raised the DSSC efficiency from 1% to 7%. DSSC separates the optical absorption and charge separation process by associating a sensitizer with a wide-band gap semiconductor of nanocrystalline morphology. Extended junction and nanostructured photoconversion devices provide the pathway for light absorption and charge collection. Advantages of nanosized semiconductor structures and particles include increased carrier lifetimes arising from space quantization, enhanced redox potentials of photogenerated holes and electron arising from increased effective band gap. It is now possible to completely depart from the classical solid state junction device by replacing the phase contacting the semiconductor by an electrolyte, thereby forming a DSSC [55].

There are the components of DSSC; a transparent conducting oxide (TCO) glass used as counter electrode-generally, a glass coated with platinum solution (its conductive site usually deposited with fluorine doped tin oxide (FTO) or indium doped tin oxide), nanostructured photoelectrode used as conducting electrode or photoanode (usually developed from TiO_2 nanoparticles), photosensitizer or dye molecule (which is anchored into the photoanode), and redox electrolyte (mostly iodide-tri iodide electrolyte) [3].

Clear glass substrates are commonly used as substrate because of their relative low cost, availability and high optical transparency in the visible and near infrared regions of the electromagnetic spectrum. Conductive coating (film) in the form of thin transparent conductive oxide (TCO) is deposited on one side of the substrate. The conductive film ensures a very low electric resistance per square. Typical value of such resistance is 10-20 Ω per square at room temperature. Before assembling the cell the counter electrode must be coated with a catalyzing layer such as graphite layer to facilitate electron donation mechanism in the electrolyte (electron donor) [54].

In the old generations of photoelectrochemical solar cells (PSC), photoelectrodes were made from bulky semiconductor materials such as Si, GaAs or CdS. However, these kinds of photoelectrodes were experienced they undergo photocorrosion when exposed to light that results in poor stability of the photoelectrochemical cells. The use of sensitized wide band gap semiconductors such as TiO_2, or ZnO_2 resulted in high chemical stability of the cell due to their resistance to photocorrosion. The problem with bulky single or poly-crystalline wide band gap is the low light to current conversion efficiency mainly due to inadequate adsorption of sensitizer and limit surface area of the electrode. One approach to enhance light-harvesting efficiency (LHE) and hence the light to current conversion efficiency is to increase surface area (the roughness factor) of the sensitized photoelectrode [54].

Due to the remarkable changes in mechanical, electrical, magnetic, optical and chemical properties of nanostructured materials compared to their phase in bulk structures, they received considerable attention [60]. Moreover, because of the area occupied by one dye molecule is much larger than its optical cross section for light capture, the absorption of light by a monolayer of dye is insubstantial. It has been confirmed that high photovoltaic efficiency cannot be achieved with the use of a flat layer of semiconductor or wide band gap semiconductor oxide surface but rather by use of nanostructured layer of very high roughness factor (surface area). Therefore, Gratzel and his coworkers replaced the bulky layer of titanium dioxide (TiO_2) with nonoporous TiO_2 layer as a photoelectrode. Also, they have developed efficient photosensitizers that are capable of absorbing wide range of visible and near infrared portion of the solar spectrum and achieved remarkable photovoltaic cell performance. Nanoporusity of the TiO_2 paste (or colloidal solution) is achievable by sintering (annealing) of the deposited TiO_2 layer at approximately 450 ºC in a well-ventilated zone for about 15 minutes. The high porosity (>50%) of the nanostructured TiO_2 layer allows facile diffusion of redox mediators within the layer to react with surface-bound sensitizers. Lindström et al. reported “A method for manufacturing a nanostructured porous layer of a semiconductor material at room temperature. The porous layer is pressed on a conducting glass or plastic substrate for use in a dye-sensitized nanocrystalline solar cell” in 2001 [61]. Because it is inexpensive, none toxic and having good chemical stability in solution while irradiated, Titanium dioxide has attracted great attention in many fields other than nanostructured photovoltaics such as photocatalysts, environmental purification, electronic devices, gas sensors, and photoelectrodes. The preparation procedure of TiO_2 film is relatively simple since it requires no vacuum facilities [62].

Moreover, nanostructured-TiO_2 layer degradation in this case is fast, and cracks form after a short period of time when the cell is exposed to direct sunlight. Recently, Zhu et al. investigated the effects of annealing temperature on the charge-collection and light-harvesting properties of TiO_2 nanotube based dye-sensitized solar cells as shown in Figure 2.1. The reported on “DSSCs containing titanium oxide nanotube (NT) arrays films annealed at 400 °C revealed the fastest transport and slowest recombination kinetics. The various structural changes were also found to have affects on the light-harvesting, charge-injection, and charge-collection properties of DSSCs, which, in turn, altered the photocurrent density, photovoltage, and solar energy conversion efficiency [63]”

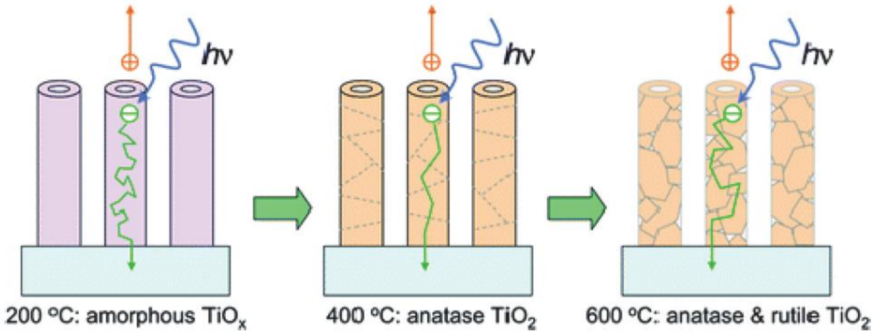

Figure 2.1 Schematic illustration of the effects of annealing temperature on the Charge-collection and light-harvesting properties of TiO_2 nanotube based dye-sensitized solar cells [63].

One of the important factors that affect the cell's efficiency is the thickness of the nanostructured TiO_2 layer which must be less than 20 μm to ensure that the diffusion length of the photoelectrons is greater than that of the nanocrystalline TiO_2 layer. TiO_2 is the most commonly used as nanocrystalline semiconductor oxide electrode in the DSSC, and it acts as an electron acceptor to support a molecular or quantum dot QD sensitizer [56]. Another wide band gap semiconductor oxide is zinc oxide (ZnO_2). ZnO_2 possesses a band gap of 3.37 eV and a large excitation binding energy of 60 meV. The nanorod array electrode showed stable photovoltaic properties and exhibited much higher energy conversion efficiency [64]. Another example, Law and coworkers have grown ZnO_2 nanowires by chemical bath deposition. ZnO_2 nanowires, 8 μm long and 100 nm diameters, were used as photoelectrode in DSSC, and the efficiency was approximately 2.4%. This low efficiency compared to that of nanostructured TiO_2 photoelectrode DSSC is probably due to inadequate surface area for sensitizer adsorption [65]. Other research groups suggested that the growth of longer, thinner, denser ZnO_2 nanowires is a practical approach to enhance cell efficiency [66]. Investigations showed that size ZnO_2 nanorods could be freely modified by controlling the parameters of solution such as temperature, precursor concentration, reaction time, and adopting multi-step growth. Nanorod structured photoelectrode offers a great potential for electron transport enhancement. It has been found that the short circuit current density and cell performance significantly increase as nanorods length increases because of a higher amount of the adsorbed dye on longer nanorods, resulting in improving conversion efficiency [64]. Because titanium dioxide is abundant, low cost, biocompatible and non-toxic, it is advantageous to be used in dye sensitized solar cells. Therefore, nanotube and nanowire-structured TiO_2 photoelectrode for dye-sensitized solar cells has been investigated. Moreover, SnO_2, or Nb_2O_5 employed not only to ensure large roughness factor (after nanostructuring the photoelectrode) but also to increase photogenerated electron diffusion length. Many studies suggest replacing nanoparticles film with an array of single crystalline nanowires (rods), nanoplants, or nanosheets in which the electron transport increases by several orders of magnitude [67].

Photosensitizers or dye molecules of proper molecular structure are used to sensitized wide band gap nanostructured photoelectrode. Upon absorption of photon, a dye molecule is oxidized and the excited electron is injected into the nanostructured TiO_2. Among the promising sensitizers, Polypyridyl compounds of Ru(II) have been investigated extensively. Besides, many researches have focused on molecular engineering of ruthenium compounds. Gratzel group developed many Ru complex photosensitizers. One famous example is the cis-Di(thiocyanato)bis(2,2'-bipyridyl)-4,4'-dicarboxylate) ruthenium(II), coded as N3 or N-719 dye. It has been an outstanding solar light absorber and charge-transfer sensitizer. In fact, for dye molecule to be excellent sensitizer, it must possess several carbonyl (C=O) or hydroxyl (-OH) groups which are capable of chelating to the Ti(IV) sites on the TiO_2 surface. Commercialized dye sensitized solar cells and modules use ruthenium bipyridyl–based dyes (N3 dyes or N917) to achieve conversion efficiencies above 10% [68].

Redox electrolyte or electrolyte containing I^-/I_3^- redox ions is used in DSSC to regenerate the oxidized dye molecules and hence completing the electric circuit by mediating electrons between the nanostructured electrode and counter electrode. NaI, LiI and R_4NI (tetraalkylammonium iodide) are well known examples of mixture of iodide usually dissolved in nonprotonic solvents such as acetonitrile, propylene carbonate and propionitrile to make electrolyte. Cell performance is greatly affected by ion conductivity in the electrolyte which is directly affected by the viscosity of the solvent. Thus, solvent with lower viscosity is highly recommended. Moreover, counter cations of iodides such as Na^+, Li^+, and R_4N^+ effect on the cell performance mainly due to their adsorption on nanostructured electrode (TiO_2) or ion conductivity. It has been found that addition of *tert*-butylpyridine to the redoxing electrolyte improves cell performance [68]. Br^-/Br_3^- redox couple was used in DSSCs and promising results were obtained. The V_{oc} and I_{sc} increased for the Eosin Y-based DSSC when the redox couple was changed from I^-/I_3^- to $Br^{-/}Br_3^-$. The redoxing electrolyte needs to be chosen such that the reduction of I_3^- ions by injection of electrons is fast and efficient. This arise from the fact that the dependence of both hole transport and collection efficiency on the dye-cation reduction and I^-/I_3^- redox efficiency at counter electrodes are to be taken into account. Besides limiting cell stability due to evaporation, liquid electrolyte inhibits fabrication of multi-cell modules, since module manufacturing requires cells be connected electrically yet separated chemically. Hence, a significant shortcoming of the dye sensitized solar cells filled with liquid state redoxing electrolyte is the leakage of the electrolyte, leading to reduction of cell's lifespan, as well as the associated technological problems related to device sealing up and hence, long-term stability. Many research groups investigate the use of ionic liquids, polymer, and whole conductor electrolytes to replace the need of organic solvents in liquid electrolytes. Despite the reported relative low cell's efficiency of 4–7.5% (device area < 1 cm^2), these kind of electrolyte are promising and may facilitate commercialization of dye sensitize solar modules [69]. Addition of polymer gel to quasi-solidify electrolytes has been investigated by many research groups. It has been found that the addition of Poly (viny1idene fluoride-co-hexafluoropropylene) to the KI/I_2 electrolyte has improved both the fill factors and energy conversion efficiency of the cells by about 17% [70]. Gel electrolytes also are very attractive from many perspectives such as: Efficiency is a compromise between electrolyte viscosity and ionic mobility; gelled ionic liquids have an anomalously high ionic mobility despite their high viscosity, and particularly for realization of monolithic arrays inter-cell sealing. Innovative classes of electrolytes such as p-type, polymeric conductor, PEDOT or PEDOT: TMA, which carries electrons from the counter electrode to the oxidized dye encouraging further investigations to optimize and/or design new ones [71].

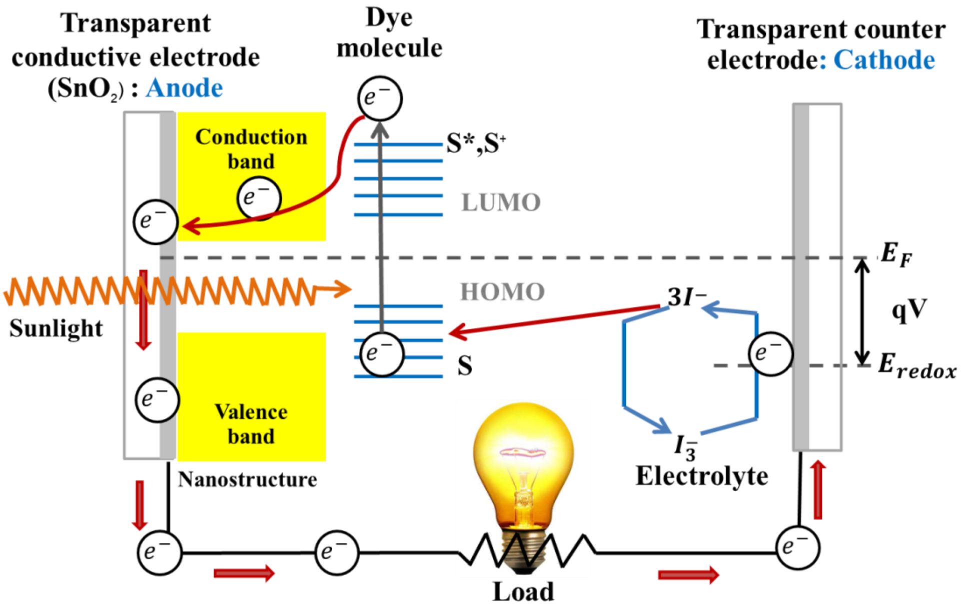

Figure 2.2 Schematic structure of DSSC [3].

Figure 2.2 illustrates the schematic structure of a dye-sensitized solar cell on the concept of DSSC operation. When sunlight irradiates on DSSC, dye molecule is excited from ground state to higher energy state as follow.

$$s + h\nu \rightarrow s^* \tag{2.1}$$

After that, dye molecule is oxidized and electron is injected into the conduction band of nanostructures according to equation 2.2.

$$s^* \rightarrow s^+ + e^- \tag{2.2}$$

Now, electron can move freely and travel to cathode. The oxidized dye molecule is regenerated by electron donation from iodide (I^-) in the electrolyte solution as follws.

$$s^+ + \frac{3}{2}I^- \rightarrow s + \frac{1}{2}I_3^- \tag{2.3}$$

Then, iodide (I^-) becomes tri iodide (I^-_3) and tri iodide (I^-_3) is regenerated to be iodide (I^-) again by reduction on cathode as shown in equation 2.4.

$$\frac{1}{2}I_3^- + e^- \rightarrow \frac{3}{2}I^- \tag{2.4}$$

All of these process can generate electrical circuit which can power devices [3].

Because of the physical nature of the dye sensitized solar cells, inexpensive, environmentfriendly materials, processing, and realization of various colors (kind of the used sensitizing dye); power window and shingles are prospective applications in building integrated photovoltaics (BIPV). The Australian company sustainable technology international has produced electric-power-producing glass tiles on a large scale for field testing, and the first building has been equipped with a wall of these glass tiles. The availability of lightweight and flexible dye sensitized cells or modules are attractive for applications in room or outdoor light powered calculators, gadgets, and mobiles. Dye sensitized solar cell can be designed as indoor colorful decorative elements. Flexible dye sensitized solar modules open opportunities for integrating them with many portable devices, baggage, gears, or outfits. In power generation, dye sensitized modules with efficiency of 10% are attractive choice to replace the common crystalline Si-based modules [54].

2.2 Structures and properties of titanium dioxide

One of methods to develop the DSSC efficiency is using of TiO_2 as photoanode in DSSCs. For example, the pure anatase TiO_2 was used in dye-sensitized solar cell. The result was found that the thickness of anatase TiO_2 photoanodes after annealing at 500 ºC was 23 µm - 41 µm. Power conversion efficiency of DSSCs performed under visible light with intensity of 100 mW/cm^2 is the highest efficiency of 3.25% [8]. In addition, the unique TiO_2 paste was used for high efficiency dye-sensitized solar cells. The result was demonstrated that titanium oxide layers possess high inner surface area and good electron transport within the layer. Overall conversion efficiencies of dye-sensitized solar cells (DSSCs) determined under standard test conditions (100 mW/cm^2, 25 °C and AM 1.5 G) are 10.2% for acetonitrile and 7.3% for ionic liquid-based electrolyte [12].

In general, titanium dioxide (TiO_2) has three phases including anatase, rutile and brookite as shown in Figure 2.3[72].

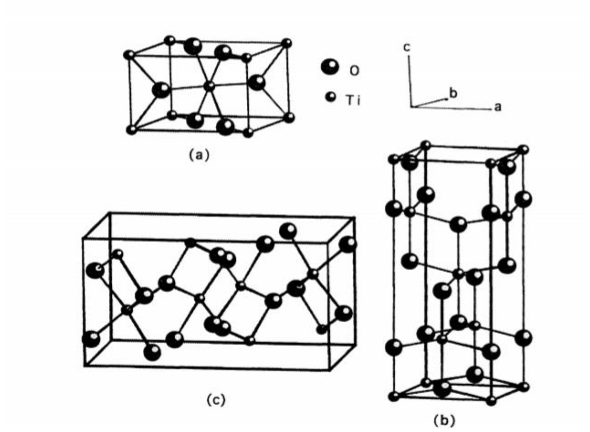

Figure 2.3 Crystal structures of TiO_2; (a) Rutile, (b) Anatase, and (c) Brookite [72].

Generally, anatase and brookite have also attracted a great deal of interest in connection with technological applications. Both rutile and anatase were intensively studied for photocatalysis and photoelectrochemical applications; however, anatase is the phase more actively investigated. It has been pointed out that the Fermi level in anatase is higher than that of rutile by about 0.1 eV. It is also known that anatase plays a key role in the injection process of photochemical solar cells with high conversion efficiency. Moreover, it has been reported that anatase thin film has different electrical and optical properties from the rutile film. The essential difference is that anatase thin film appears to have a wider optical absorption gap and a smaller electron effective mass, resulting in a higher mobility for the charge carriers. These properties are beneficial to further applications in optoelectronic and other devices [72].

Titania properties depend on the crystallinity and isomorph type, and hence the utility of their application also varies. For example, anatase phase is preferred in charge-separating devices such as dye-sensitized solar cells (DSSCs) and in photocatalysis, while rutile is used predominantly in gas sensors and as dielectric layers of the titania polymorphs because of its minimum free energy. Other polymorphs including anatase transform into rutile through a first-order phase transformation. The temperature at which metastable anatase converted to rutile depends on several factors including the presence of impurities, feature size, texture, and strain. Hence with sintering, porosity and/or surface area reduction occur due to nucleation-growth type of phase transformations [72].

The crystal parameters, the Ti-O interatomic distances, and the O—Ti—O bond angles for the three phases are summarized in Table 2.3. Rutile and anatase are both tetragonal, containing six and twelve atoms per unit cell, respectively. In both structures, each Ti atom is coordinated to six O atoms and each O atom is coordinated to three Ti atoms. In each case, the TiO_6 octahedron is slightly distorted, with two Ti—O bonds slightly greater than the other four, and with some of the O—Ti—O bond angles deviating from 90°. The distortion is greater in anatase than in rutile. The structure of rutile and anatase crystals has been described frequently in terms of chains of TiO_6 octahedra having common edges. Two and four edges are shared in rutile and anatase, respectively [72].

Table 2.3 The data of TiO_2 crystal structures [72].

	Rutile	**Anatase**	**Brookite**
Crytal structure	tetragonal	tetragonal	orthorhombic
Lattice constants (Å)	a = 4.5936 c=2.9587	a = 3.784 c = 9.515	a = 9.184 b = 5.447 c = 5.145
Space group	$P4_2$/mm	I41/amd	Pbca
Molecule/cell	2	4	8
Volume/molecule(Å^3)	31.2160	34.061	32.172
Density (g/cm^3)	4.13	3.79	3.99
Ti─O bond angle (Å)	1.949(4) 1.980(2)	1.937(4) 1.965(2)	1.87~2.04
O─Ti─O bond angle	81.2° 90.0°	77.7° 92.6°	77.0°~105°

The third form of TiO_2, brookite shown in Figure 2.3c , has more complicated structure. It has eight formula units in the orthorhombic cell. The interatomic distances and the O—Ti—O bond angles are similar to those of rutile and anatase. The essential difference is that there are six different Ti—O bonds ranging from 1.87 to 2.04 Å. Accordingly, there are twelve different O—Ti—O bond angles ranging from 77º to 105º. In contrast, there are only two kinds of Ti—O bonds and O—Ti—O bond angles in rutile and anatase. We can also envision brookite as formed by joining together the distorted TiO_6 octahedra sharing three edges [72].

The prototypical photocatalyst TiO_2 exists in different polymorphs, and the most common forms are the anatase and rutile crystal structures. Generally, anatase is more active than rutile. The band gap of TiO_2 is larger than 3 eV (3.0 for rutile and 3.2 for anatase), thus making pure TiO_2 primarily active for UV light. However, for pure phases it is generally accepted that anatase exhibits a higher photocatalytic activity compared to rutile TiO_2. Furthermore, not only these two polymorphs show varying photoactivity but also the different crystallographic orientations of the same material may exhibit different activities. Anatase has a larger band gap than rutile TiO_2. While this reason reduces the light that can be absorbed, it may raise the valence band maximum to higher energy levels relative to redox potentials of adsorbed molecules. This increases the oxidation 'power' of electrons and facilitates electron transfer from TiO_2 to adsorbed molecules. This explanation has also been expanded to explain surface orientation dependent activities by suggesting that different surfaces exhibit different band gaps [73]. Moreover, Anatase phase is exceptional in photo catalytic activity due to its high reflection index, low extinction coefficient, non-toxicity, high chemical and physical stability and low cost [35].

Highly crystalline structures offer unique advantages over amorphous architectures by providing a direct and rapid pathway for charge transport, thus decreasing the carrier path length, which in turn reduces recombination losses

2.3 Fabrication of TiO_2 nanotube arrays by electrochemical anodization

There are a number of ways to fabricate TiO_2 nanostructures such as hydrothermal synthesis [36], chemical vapor deposition [37], atmospheric pressure plasma jet [38], electrospinning [39], atomic layer deposition [40], and etc. TiO_2 nanotubes are fabricated by anodization process which is renowned for its uncomplicated process.

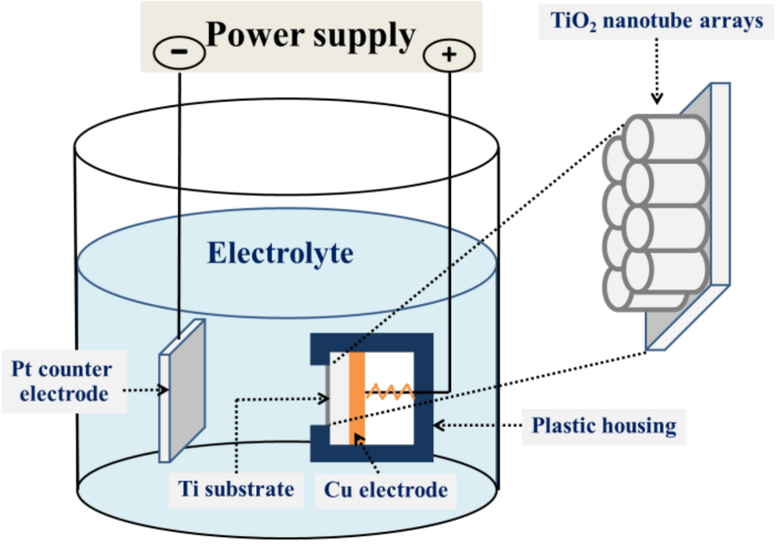

Figure 2.4 Schematic representation of anodization setup [71].

Anodization method is the system which consists two-electrode configuration. The anode or working electrode is Ti substrate which mounted onto plastic housing apparatus to be anodized and the cathode or counter electrode is highly pure platinum. This apparatus allows only one face of the titaniun substrate contacts with electrolyte solution to obtain TiO_2 nanotubes as shown in Figure 2.4 [74].

The pore formation of TiO_2 nanotubes can be explained by as follows. After anodization process, oxide films are created over Ti surface due to the interaction of the Ti metal with O^{2-} or OH^- ions and formed initial oxide layers which could be described as follows:

$$2H_2O \rightarrow O_2 + 4e^- + 4H^+ \tag{2.5}$$

$$Ti + O_2 \rightarrow TiO_2 \tag{2.6}$$

Oxide layer is etched by NH_4F solution. Under application of electric field, metal ions of Ti^{4+} migrate from the metal/oxide interface and move towards the oxide/electrolyte interface. The reaction is written as follows:

$$TiO_2 + 6F^- + 4H^+ \rightarrow TiF_6^{2-} + 2H_2O \qquad (2.7)$$

After that, the pores of TiO_2 spread uniformly over the surface thus the formation of TiO_2 nanotubes is created [37].

Numerous experimental evidences suggest that TiO_2 nonotubes possess the exceptional properties, for example, high electron transport, large electron diffusion length, and relative band-edge position which are suitable to trigger a wide range of photocatalytic reaction [41, 42].

In general, the mechanism of TiO_2 nanotube formation in fluorine-ion based electrolytes is said to occur as a result of three simultaneous processes: the field assisted oxidation of Ti metal to form titanium dioxide, the field assisted dissolution of Ti metal ions in the electrolyte, and the chemical dissolution of Ti and TiO_2 due to etching by fluoride ions, which is enhanced by the presence of H^+ ions. TiO_2 nanotubes are not formed on the pure Ti surface but on the thin TiO_2 oxide layer naturally present on the Ti surface. Therefore, the mechanism of TiO_2 nanotubes formation is related to oxidation and dissolution kinetics. Schematic diagram of the formation of TiO_2 nanotubes by anodization process is shown in Figure 2.5. The mechanism of nanotube structure formation in anodization can be described as follows:

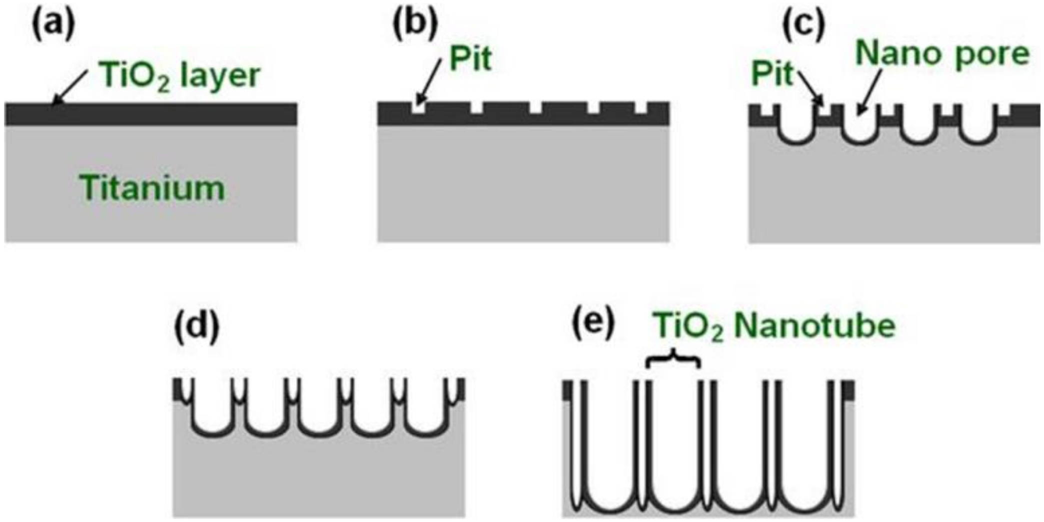

Figure 2.5 Schematic illustration of TiO_2 nanotube formation; (a) Before anodization, a nano scale TiO_2 passivation layer is on the Ti surface, (b) When constant voltage is applied, pits are formed on the TiO_2 Layer, (c) As anodization time increases, pits grow longer and larger, and then become nanopores, (d) Nanopores and small pits undergo continuous barrier layer formation, (e) After specific anodization time, completely developed nanotubes are formed on the Ti surface [75].

Highly ordered, vertically oriented TiO_2 nanotube-arrays fabricated by potentiostatic anodization of titanium constitute a material architecture that offers a large internal surface area without a concomitant decrease in geometric and structural order. The precisely oriented nature of the nanotube array, makes them excellent electron percolation pathways for vectorial charge transfer between interfaces.

It is now well established that the properties of the nanotube arrays are dependent upon their specific architecture, including length, wall thickness, wall roughness, pore diameter, and tube-to-tube spacing. The geometrical features of the nanotube arrays are controlled by a variety of parameters that are not specific to one geometrical feature, including anodization potential, electrolyte composition and properties thereof (conductivity, viscosity), as well as anodization time and temperature. Virtually identical tubes can be obtained in dissimilar electrolytes by the control of different anodization variables [75]

2.4 Doped titania nanotubes

Titania nanotube arrays appear a useful catalyst, under band gap illumination, for water photoelectrolysis. Semiconducting TiO_2 (3.2 eV band gap) absorbs UV light, which comprises only approximately 4% of the solar energy spectrum. Means to shift the absorption properties of TiO_2 have historically focused on sensitization of the TiO_2 with low band gap semiconductors having suitable energy level positions with respect to that of TiO_2, or by doping with foreign elements such as Mg, Mg-Nb, Cu, S, Fe, Ni, Co, Zn, Na, CdTe [43-48].

In order to enhance the performance of TiO_2, it must be improved by doping some elements. Previous research has been conducted to improve the performance of TiO_2. For example, the transition-metal-doped TiO_2 nanotubes are highly visible-active and stable, excellent photoelectrochemical properties, and photocatalytic activities under visible light irradiation [76, 77]. Further, The Fe^{3+} doped TiO_2 nanotubes synthesized by a solvothermal method in $FeCl_3$ solution indicate significant enhancement of the visible light absorption and exhibit excellent photocurrent and photoelectrochemical performance [78].

Here, this study contributes to the enhancement of TiO_2 nanotubes in dye-sensitized solar cell applications and presents the investigation of the effect of potassium ferricyanide ($K_3[Fe(CN)_6]$) on TiO_2 nanotubes. In photoelectrochemical solar cell applications, $K_3[Fe(CN)_6]$ is widely used as photoelectroactive electrolyte, because it comprises K, Fe, C, and N which have high potential for improvement on the performance of TiO_2 nanotubes. The result demonstrated that the conversion of solar energy to electrical energy efficiency in n-CdSe ferro/ferricyanide pho toelectrochemical solar cells increases when the pH of ferro/ferricyanide electrolyte is increased. Ferro/ferricyanide speciation represented that, in the alkaline pH region where ferrocyanides are most photoelectroactive, cationic complexes of cesium ferro/ferricyanide electrolytes showed high photoelectrochemical cell. Moreover, The photoelectrochemistry at n-CdSe of the alkaline potassium ferro/ferricyanide electrolyte also showed the highest conversion efficiencies. Iron pentacyano-ligand redox complexes studied, electrolytes based on the simple iron hexacyano complex were shown to maximize the kinetics of photo-driven n-CdSe charge transfer [79].

CHAPTER 3

EXPERIMENTAL PROCEDURES

This chapter explains the synthesis of highly ordered titania nanotubes via one-faced and single-step anodization method and the characterization of the obtained samples using XRD, SEM, AFM, XPS, EDS and UV-visible spectroscopy. Moreover, the fabrication of dye-sensitized solar cells using titania nanotube samples as photoanodes will be presented.

3.1 Preparation of TiO_2 nanotubes and $K_3[Fe(CN)_6]$ doped TiO_2 nanotubes

The 0.25 mm thick titanium foils (99.7% purity) as shown in Figure 3.1 (a) and all chemicals were purchased from Sigma Aldrich as shown in Figure 3.1 (b). Prior to anodization as shown in Figure 3.3, the titanium foils were polished in a solution containing deionized water and ethanol by ultrasonic cleaned for 40 min as shown in Figure 3.1 (c) and then dried under a flowing air stream. Anodic growth experiments were performed by potentiostatic anodization in a conventional two-electrode compartment electrochemical cell. Then, the pretreated Ti sheet will be used as a working electrode (anode) and highly pure platinum sheet was used as counter electrode (cathode). The anodization was performed in ethylene glycol based electrolyte consisting of 0.25 wt%NH_4F and 2 vol% H_2O at applied voltage of 50 V for 2 h at ambient temperature. The separation between the electrodes was 2 cm which made electric field of 2,500 V/m.

Titania nanotube samples were doped by potassium ferricyanide ($K_3[Fe(CN)_6]$), 99.0% purity) via anodization process. Anodization was conducted in an ethylene glycol solution consisting of 0.25 wt% NH_4F and 2 vol% H_2O, which was kept constant while the concentrations of $K_3[Fe(CN)_6]$ were varied from 0.05 wt% to 0.20 wt% with increment of 0.05 wt% at applied voltage of 50 V for 2 h at ambient temperature as shown in Figure 3.2 and Table 3.1. After anodization, the obtained samples were cleaned immediately with pure water using ultrasonic cleaner and then dried in the air stream. The prepared samples were annealled at 450 °C for 2 h in order to transform the amorphous titania to nanocrystalline anatase using chamber furnace as shown in Figure 3.4.

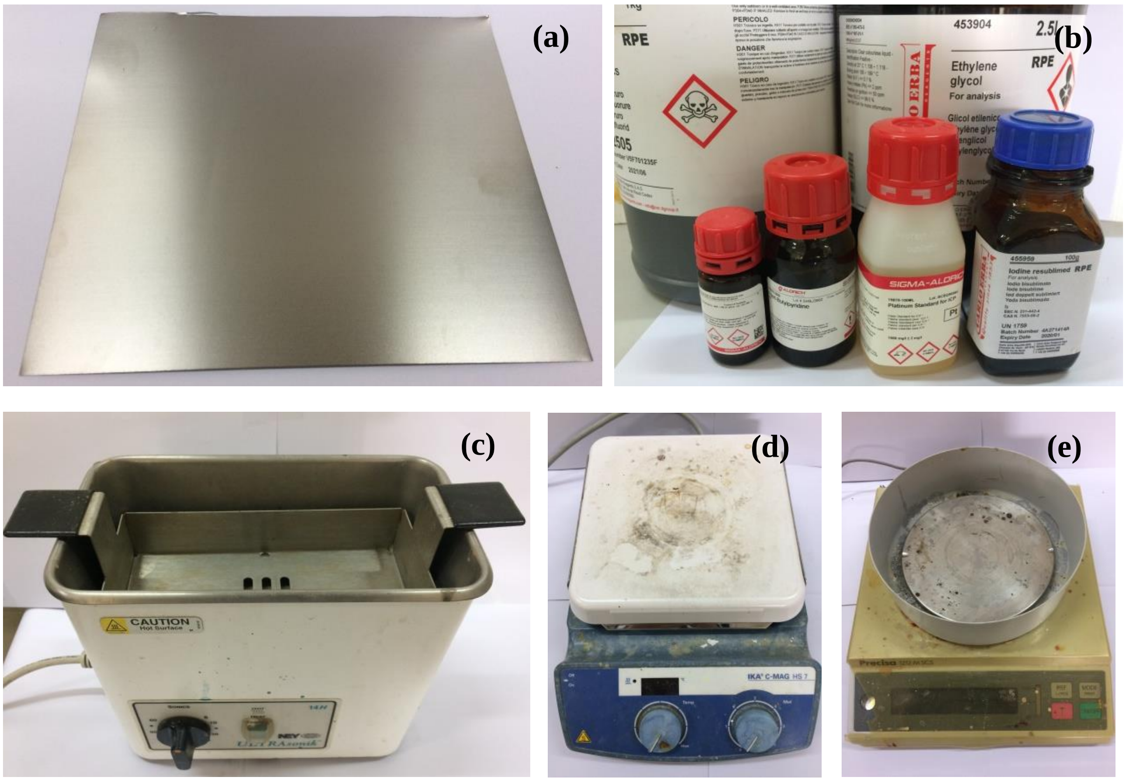

Figure 3.1 (a) Ti sheet, (b) Chemicals, (c) Ultrasonic cleaner, (d) Magnetic stirrer and (e) Weighing machine.

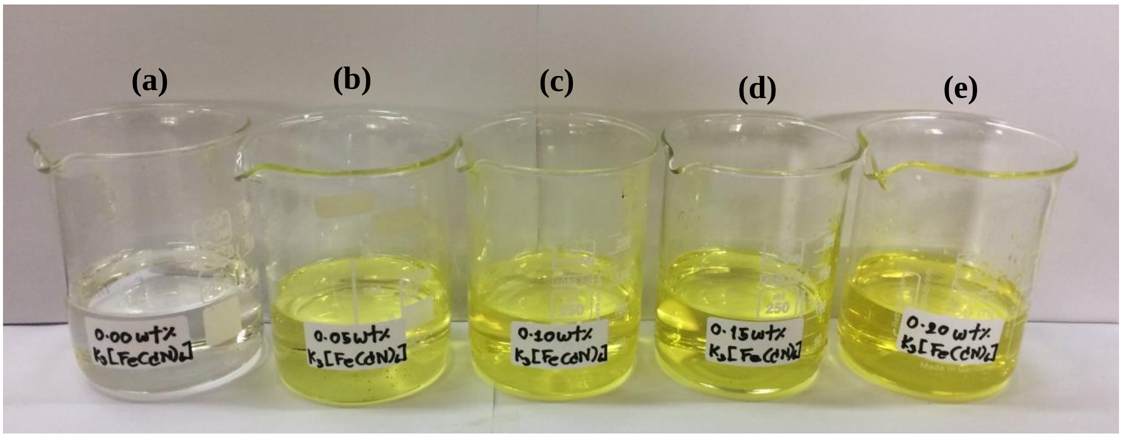

Figure 3.2 Anodizing electrolytes of (a) undeped electrolyte solution, (b) 0.05 wt% $K_3[Fe(CN)_6]$ doped electrolyte, (c) 0.10 wt% $K_3[Fe(CN)_6]$ doped electrolyte, (d) 0.15 wt% $K_3[Fe(CN)_6]$ doped electrolyte and (e) 0.20 wt% $K_3[Fe(CN)_6]$ doped electrolyte.

Table 3.1 The compositions of anodizing electrotytes.

Anodizing electrolytes	**Chemical compositions**			
	Ethylene glycol: EG (ml)	**NH_4F (wt%)**	**DI-water (vol%)**	**$K_3[Fe(CN)_6]$ (wt%)**
(a)	100	0.25	2.00	0.00
(b)	100	0.25	2.00	0.05
(c)	100	0.25	2.00	0.10
(d)	100	0.25	2.00	0.15
(e)	100	0.25	2.00	0.20

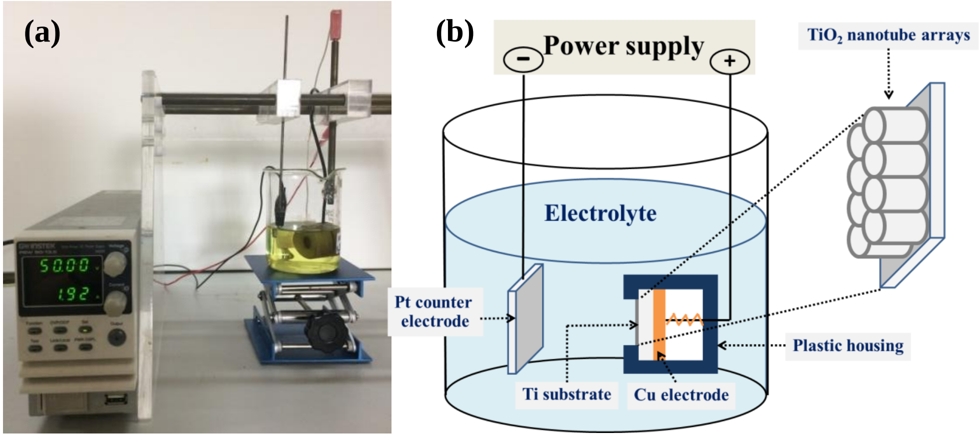

Figure 3.3 **(a) DC anodizing apparatus and (b) Schematic representation of anodization setup.**

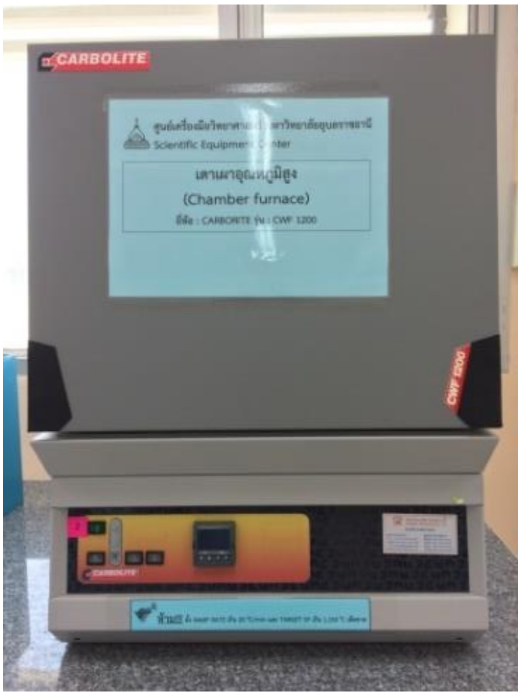

Figure 3.4 **CARBORITE CWF 1200 chamber furnace.**

3.2 Characterizations of the obtained samples

The crystalline structures of the obtained samples were analyzed using X-ray diffraction (XRD). The surface morphology of un-doped and doped TiO_2 nanotube samples was examined using scanning electron microscopy (SEM), and the surface roughness parameters values of all samples were carried out by means of atomic force microscopy (AFM). UV- Vis diffuse reflectance spectra of all anodized samples were recorded using UV-Vis spectroscopy. Elemental analysis of titania nanotube arrays was determined using X-ray photoelectron spectroscopy (XPS) and energy dispersive X-ray spectroscopy (EDS).

X-ray diffraction (XRD)

The crystalline structures and XRD patterns of the obtained nanotube samples were analyzed using Philips X’ Pert MPD diffractometer as show in Figure 3.5. The Cu-K_α radiation with wavelength of 0.154 nm was used. The operational voltage and current were 40 kV and 40 mA, respectively. The spectral angles were scan in 2θ from 20 °- 80 ° at rate of 0.02° per second.

Figure 3.5 Philips X-Pert-MDP X-ray diffractometer.

X-ray diffraction (XRD) is nondestructive technique to investigate the structure parameters of crystalline material such as crystal structure, phases, average grain size, crystallinity, strain, and crystal defects. X-ray diffraction peaks are produced by constructive interference of a X-ray monochromatic beam scattered at specific angle from each set of lattice planes in a sample. The peak intensities are determined by the distribution of atoms within the lattice. Consequently, the X-ray diffraction pattern is the fingerprint of periodic atomic arrangements in a given material.

A cathode ray tube generates X-rays and then it is filtered to produce monochromatic radiation, collimated to concentrate, and directed toward the sample in Figure 3.6.

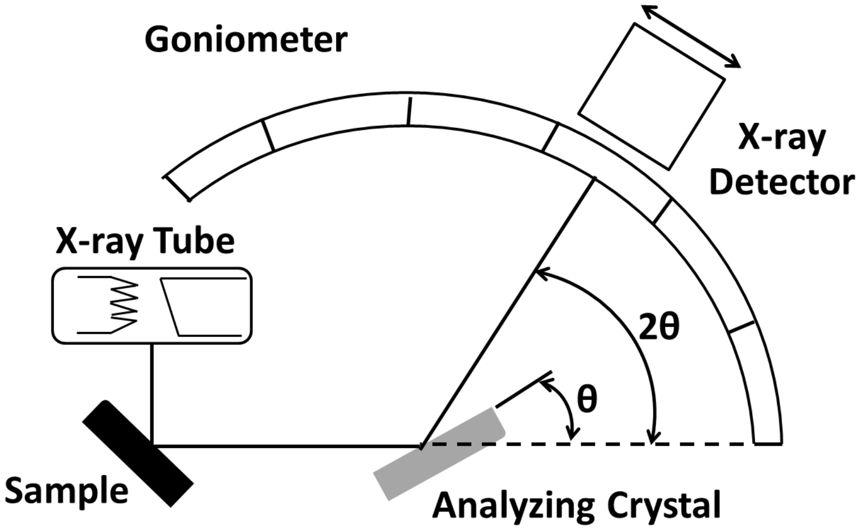

Figure 3.6 Schematic diagram of a diffractometer system.

The interaction of the incident rays with the sample produces constructive interference (and a diffracted ray) when conditions satisfy Bragg's Law [80]:

$$n\lambda = 2d \sin\theta \quad (3.1)$$

where, n is an integer, λ is the wavelength of the X-rays, d is the interplanar spacing generating the diffraction, and θ is the diffraction angle.

This formula relates to the wavelength of electromagnetic radiation and the diffraction angle and the lattice spacing in a crystalline sample. These diffracted X-rays are then detected, processed and counted. By scanning the sample through a range of 2θ angles, all possible diffraction directions of the lattice should be attained due to the random orientation of the powdered material. Conversion of the diffraction peaks to d-spacing allows identification of the compound because each compound has a set of unique d-spacing. Typically, this is achieved by comparison of d-spacing with standard reference patterns.

Scanning Electron Microscopy (SEM)

The surface morphology of un-doped and doped TiO_2 nanotube samples was examined using scanning electron microscopy (SEM)**.** SEM analysis was carried out in a JEOL JSM-6010LV Scanning Electron Microscope as shown in Figure 3.7.

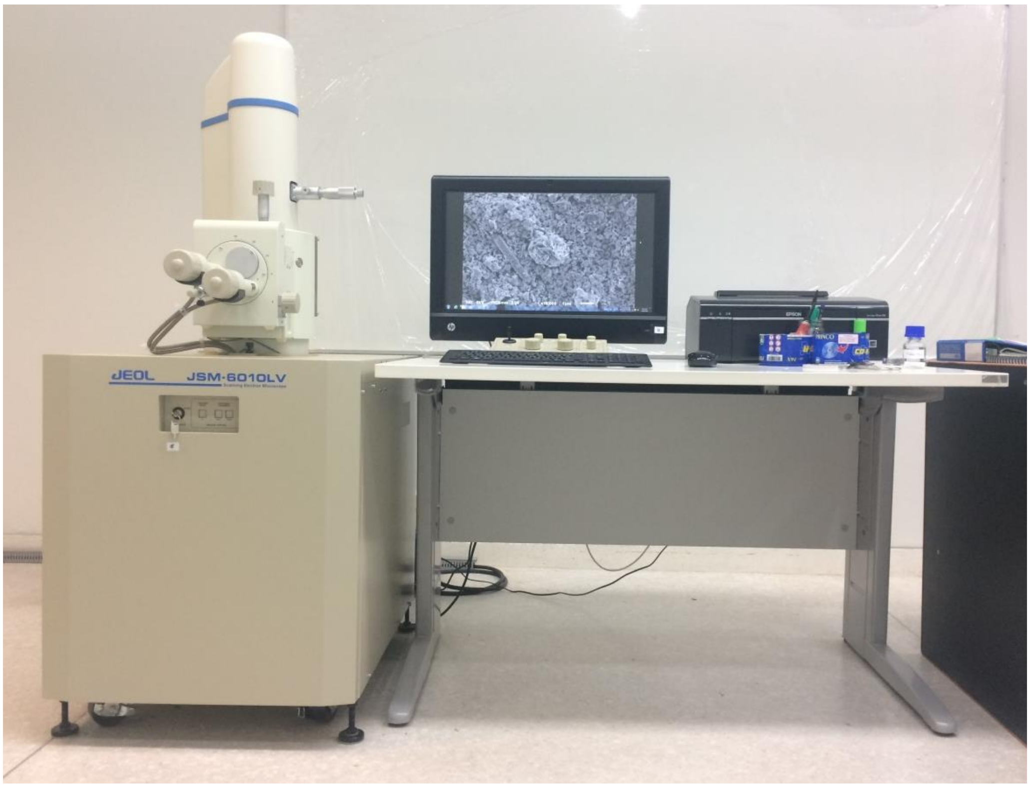

Figure 3.7 JEOL JSM-6010LV Scanning Electron Microscope.

The microscope in scanning electron microscopy (SEM) presents a higher complexity level than that of an optical microscope (OM), as shown in Figure 3.8, which schematically depicts the OM and the SEM optical systems.

In SEM, a highly energetic and focused electron beam is formed and scans the specimen in a raster scan pattern. Then, different effects can result from the interaction between the electron beam and the electrons in the sample.

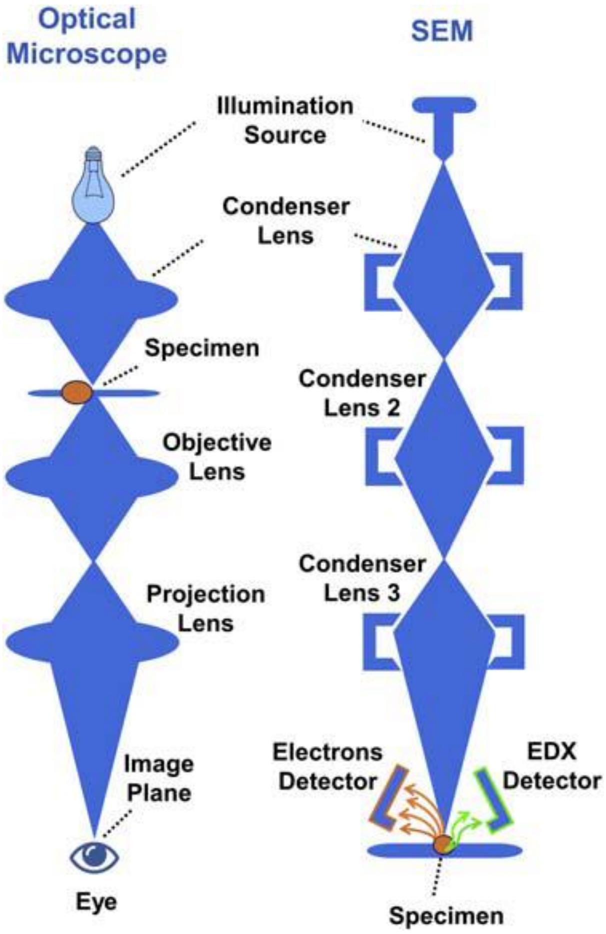

Figure 3.8 Scheme showing the optical systems for optical-light microscopy and scanning electron microscopy [81].

Part of the electron beam will be un-scattered, though most of the electron beam interacts with the specimen and undergoes inelastic and elastic scattering. In the first case, the direction of the primary electrons is changed but their overall energy is maintained. Inelastic scattered electrons change their direction and lose part of their energy. Although most of the electron beam energy transform into heat in the specimen, other events occur and are detected outside the specimen: secondary effects. Subsequent effects can include emitted secondary electrons, backscattered electrons and characteristic X-rays. The secondary electrons are generated when an incident electron changes its path and loses part of its energy, which is transferred to an atom in the specimen (inelastic event) and leaves the sample with a very small energy. Each primary or incident electron can produce several secondary electrons, thus secondary electrons are abundant and the most used imaging signal in SEM. Backscattered electrons result from the collision between an incident electron and an atom in the specimen and losing part of its energy and being scattered ‘backwards’ 180 degrees. Some of the backscattered electrons can generate more secondary electrons when exiting the specimen. The production of backscattered electrons varies directly with the atomic number of the chemical elements present in the specimen: the higher the atomic number, the brighter that region will appear. X-rays emission results from the deenergization of an atom in the sample after a secondary electron is produced. This signal is extremely important for analytical purposes. A key factor in SEM is the interaction volume, the region into which the electron beam penetrates the specimen, i.e., the three-dimensional volume resulting from the interaction of the electron beam with the specimen atoms. The emission depth of the different signals used in SEM is influenced by the electron beam energy, specimen nature, composition and sample preparation. The higher the accelerating voltage applied on the electron beam, the larger the interaction volume. In SEM, imaging is carried out by using the emission of secondary electrons (topography) and backscattered electrons (atomic number). Analytical X-rays enable qualitative and quantitative analysis of the specimens. Thus, SEM images provide information on the topography, morphology, composition and crystallographic nature of the analyzed specimens. Though electron and optical microscopes share some common principles, the differences are rather evident as shown in Table 3.2.

SEM offers a great deal of information and surpasses most of the limitations of optical microscopy. For samples highly sensitive to the electron beam such as biological samples or synthetic organic polymer materials, there are two alternatives to the conventional SEM, the low-voltage microscope and the environmental SEM

(ESEM). The former enables imaging down to a few tens of volts with fairly high resolution proving to be particularly useful for charge reduction. On the other hand, lower voltage and high beam current necessary for EDS analysis and detection of certain elements are more problematic. ESEM is a conventional SEM that operates from lower pressures up to, at least, the pressure required to observe liquid distilled water. This microscope allows imaging of uncoated samples since accumulated electrical charges and even electrons from the electron beam are scattered by collision with the gas molecules inside the microscope chamber. Moreover, the combination of SEM imaging and elemental qualitative/quantitative analysis given by EDS made it into one of the most powerful tools in scientific research [81].

Table 3.2 Summary of the main differences between optical and electron microscopy [81].

Optical-light Microscopy	**Scanning Electron Microscopy**
Illumination source	
Light rays	Electron beam
Resolution	
Below 0.25 µm up to 0.25 µm	Down to 0.4 nm
Magnification/depth of field	
500x to 1500x	2000000x
Small	Large
Lenses material/vacuum	
Optical glass/no need for vacuum	Electromagnets/high vacuum in needed
Image dimension/colour	
2D/3D	2D/3D
RGB	Grey scale
Specimen preparation	
Simple	Difficult
Applications	
Live/dead specimens	Dead and dried specimens

Table 3.2 Summary of the main differences between optical and electron microscopy (continued) [81].

Cost/maintenance	
Cheap/negligible	Very expensive
Chemical composition: qualitative/ quantitative analysis	
Unavailable	Available and accurate (the latter depends on sample preparation and equipment operation)

Atomic Force Microscopy (AFM)

The surface roughness parameter values of all samples were carried out by Park System XE-100 Atomic Force Microscope (AFM) as shown in Figure 3.9.

Figure 3.9 Park System XE-100 Atomic Force Microscope.

The AFM principle is based on the cantilever/tip assembly that interacts with the sample; this assembly is also commonly referred to as the probe. The AFM probe interacts with the substrate through a raster scanning motion. The up/down and side to side motion of the AFM tip as it scans along the surface is monitored through a laser beam reflected off the cantilever. This reflected laser beam is tracked by a position sensitive photo-detector (PSPD) that picks up the vertical and lateral motion of the probe. The deflection sensitivity of these detectors has to be calibrated in terms of how many nanometers of motion correspond to a unit of voltage measured on the detector.

In order to achieve the AFM modes known as tapping modes, the probe is mounted into a holder with a shaker piezo. The shaker piezo provides the ability to oscillate the probe at a wide range of frequencies (typically 100 Hz to 2 MHz). Tapping modes of operation can be divided into resonant modes (where operation is at or near the resonance frequency of the cantilever) and off-resonance modes (where operation is at a frequency usually far below the cantilever's resonance frequency).

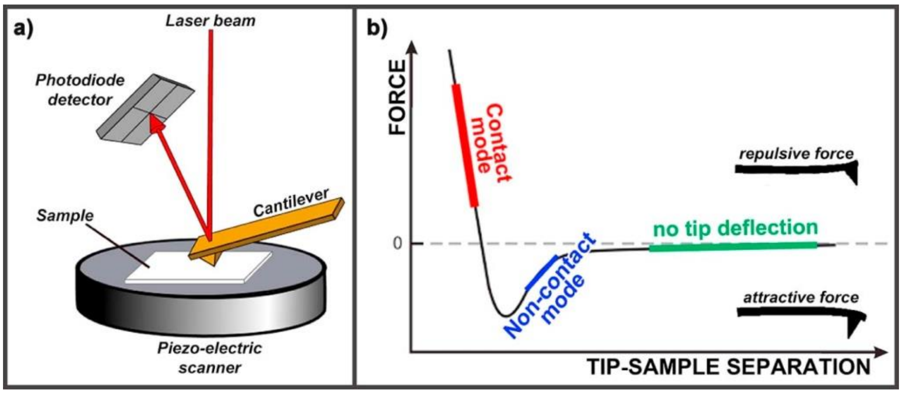

Figure 3.10 Atomic force microscopy. a) Schematic presentation of AFM; b) Force regimes governing AFM measurement [82].

A schematic representation of the basic AFM set-up is shown in Figure 3.10a. When using AFM a tip attached to a flexible cantilever moves across the sample surface, measuring the surface morphology on the atomic scale. The force between the tip and the sample is measured during scanning, by monitoring the deflection of the cantilever.

AFM can work in two modes, namely contact and non-contact modes. In contact mode the repulsive van der Waals forces are measured between the atom in the tip and the atoms of the material surface. Consequently, the tip is in physical contact with the surface during the analysis and can cause physical damage to soft material. In non-contact mode the attractive van der Waals is measured by oscillating the cantilever at its resonance frequency from the sample surface. Because non-contact mode measures the weaker attractive forces the lateral resolution is less than that achieved with contact mode as presented in Figure 3.10b.

UV-Vis Spectroscopy

UV- Vis diffuse reflectance spectra of all anodized samples were recorded using UV-Vis spectroscopy. The UV absorption spectrum using a Perkin Elmer Lamda 35 UV-Visible Spectrophotometer as shown in Fugure 3.11.

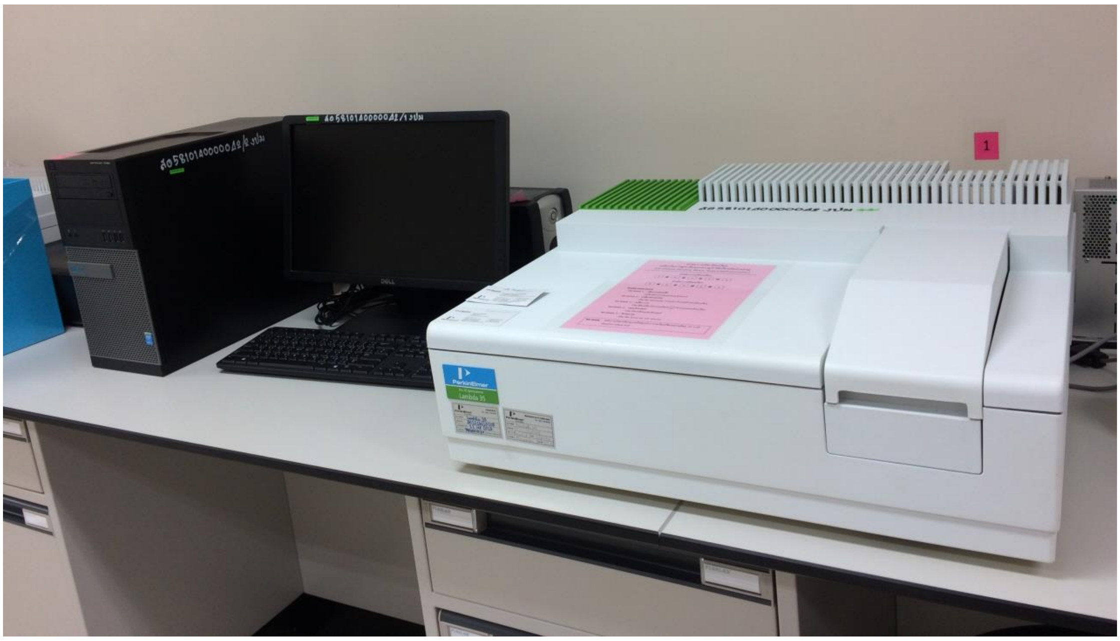

Figure 3.11 Perkin Elmer Lamda 35 UV-Visible Spectrophotometer.

Ultraviolet Visible (UV/Vis) spectrophotometer is a technique used to quantify the light that is absorbed and scattered by a sample (a quantity known as the extinction, which is defined as the sum of absorbed and scattered light). In its simplest form, a sample is placed between a light source and a photodetector, and the intensity of a beam of light is measured before and after passing through the sample. These measurements are compared at each wavelength to quantify the sample’s wavelength dependent extinction spectrum. The data is typically plotted as extinction as a function of wavelength. Each spectrum is background corrected using a “blank” – a cuvette filled with only the dispersing medium – to guarantee that spectral features from the solvent are not included in the sample extinction spectrum.

The optical band gap energy samples were calculated using a Tauc plot of the modified Kubelka- Munk (MK) function with a linear extrapolation [83-86] as given below.

$$(\alpha h\upsilon)^{1/2} = \beta(h\upsilon - E_g) \qquad (3.2)$$

where, E_g is the Tauc optical band gap, α=2.303A/d (A is optical intensity, and d is thickness of the sample), ν is the frequency of incident light, β is a constant which depends on the width of the localized states in the band gap and h is Planck's constant.

X-ray Photoelectron Spectroscopy (XPS)

The chemical composition of sample surface was investigated by X-ray photoelectron spectrometer (XPS; AXIS ULTRADLD, Kratos analytical, Manchester UK.) The base pressure in the XPS analysis chamber will be about 5×10^{-9} torr. The samples are excited with X-ray hybrid mode 700x300 µm spot area with a monochromatic Al Kα 1,2 radiation at 1.4 keV. X-ray anode will run at 15kV 10mA 150 W. The photoelectrons are detected with a hemispherical analyzer positioned at an angle of 90^{o} with respect to the normal to the sample surface. The spectra are calibrated using the C 1s line (BE=285 eV), XPS Software = VISION II by Kratos analytical co.,ltd as shown in Figure 3.12.

Figure 3.12 AXIS ULTRADLD, Kratos analytical, Manchester UK X-ray photoelectron spectrometer.

X-ray photoelectron spectroscopy (XPS), also known as electron spectroscopy for chemical analysis (ESCA), is a sensitive quantitative spectroscopic technique for analyzing the surface chemistry of a material. XPS spectra are obtained by irradiating a material with a beam of X-rays such as a typical Al K_{α} or Mg K_{α} sources, while simultaneously measuring the kinetic energy and number of electrons that escape from atoms on the surface of the material being analyzed. Using the intensity of the electron escaping from the surface and the binding energy (calculated from the measured kinetic energy recorded), an XPS spectrum is obtained. In XPS surface analysis, a UHV system is needed in order to obtain the maximum electron count during the acquisition of spectra because the analyzer is usually one meter away from the X-ray irradiated surface. The ultra-high vacuum (UHV) surface analytical technique qualitatively and quantitatively estimates the elemental composition of elements with an atomic number of lithium and above, in addition to identifying the types of chemical bonds and oxidation state in the material surface. XPS has been extensively applied to study surface chemistry in a wide variety of fields, such as electronics, forensics and biology. Nevertheless, since conventional XPS must maintain a UHV environment, the method is limited to solid samples and focuses on examining surfaces of semiconductors, thin films and [87].

Energy Dispersive X-ray Spectroscopy (EDS)

Elemental analysis of titania nanotube arrays was determined using energy dispersive X-ray spectroscopy (EDS). In this work an OXFORD LINK ISIS 300 Energy Dispersive X-ray System was used as shown in Figure 3.13.

Figure 3.13 OXFORD LINK ISIS 300 Energy Dispersive X-ray System inside JEOL JSM-5410LV SEM.

X-rays are highly energetic photons resulting from electronic transitions in the atoms of a targeted solid by an incident accelerated electron beam. Typically, the incident electron collides with an atom of the specimen and ejects an electron from the K-shell (n ¼ 1 shell) of the metal, and a vacancy or hole is left in that shell. If an electron from another shell fills in that vacancy (electron transitions), then X-rays are emitted. Electronic transitions to the K-shell (n ¼ 1) are named KX-rays, those to the L-shell (n ¼ 2) are LX-rays and to the M-shell (n ¼ 3) are the MX-rays. These transitions are characteristic of each chemical element and this is the main reason that led to the development of EDS detection systems in electron microscopy and consequently widening its use in materials microstructural characterization. Refering to previous description, the interaction volume and the volume from which the X-rays are generated are key factors for the quality of the final EDS spectrum. Moreover, the amount of generated signal strongly depends on the energy of the X-rays and the average atomic weight of the sample. For example, X-rays such as carbon K_α are easily absorbed by the solid sample and only a few are detected. In contrast, harder X-rays such as iron K_α are able to rupture the solid specimen and only a small amount is absorbed.

These characteristic X-rays are the analytical signals used in electron microscopy for chemical analysis. An X-ray spectrum emitted by the specimen provides both qualitative and quantitative information, allowing identification of which elements present in the sample and the amount of each element. In addition to the emitted X-rays, a small amount of secondary X-rays can also be induced when the primary X-rays pass through the specimen and interact with the atoms of the sample.

The spatial resolution of X-ray microanalysis is the smallest distance between two volumes from which independent X-ray microanalyses are obtained. Since the interaction volume depends on the incident beam diameter as well as the spreading of the beam caused by elastic scattering of the beam within the sample, then microanalysis spatial resolution will strongly depend on the specimen. On the other hand, increasing spatial resolution compromises the limit of detection for a particular chemical element. The higher the spatial resolution, the smaller is the analyzed volume and, consequently, the smaller is the signal intensity [81].

3.3 Assembly of DSSCs

The active areas (0.25 cm^2) of anodized samples will be used as photoanodes and immersed in acetonitrile solution containing 5×10^{-4} M cis-bis (isothiocyanato)-bis ($2,2^{/}$ bipyridyl-$4,4^{/}$ dicarboxylato) ruthenium (II) bis-tetrabutyl-ammonium (N719) dye as shown in Figure 3.14a for 24 hours. After that, all samples will be washed with ethanol and dried in an oven with temperature at 80 °C for 30 minutes. For Pt counter electrode, the transparent conductive oxide glass slides (TCO) with conductive side will be cleaned with alcohol solution by ultrasonic cleaner for 15 minutes and rinsed with deionized water. TCO glass slides will be deposited with the drop of platinum solution (H_2PtCl_6) and annealed at 450 °C for 2 hours as shown in Figure 3.14b. The iodide/triiodide (I^-/I_3) electrolyte will be prepared by mixed solvent of 0.7 M lithium iodide (LiI), 0.04 M iodine (I_2), 0.05 4-tertbutypyridine in acetonitrile as shown Figure 3.14c[74]. Finally, photoelectrode samples and Pt counter electrodes will be assembled with binder clips and injected with the LiI/Iodine electrolytes into the hole between them in order to obtained dye-sensitized solar cells (DSSCs) devices as shown in Figure 3.15.

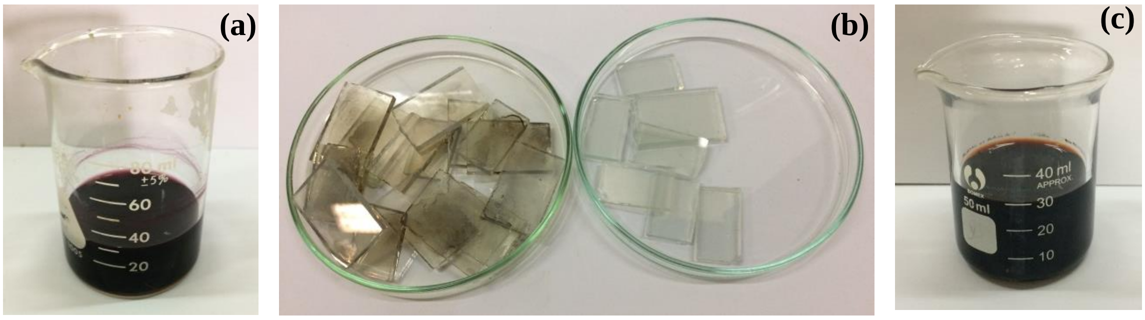

Figure 3.14 (a) acetonitrile solution containing 5×10^{-4} M N719 dye, (b) transparent conductive oxide glass slides (TCO), and (c) iodide/triiodide (I^-/I_3) electrolyte.

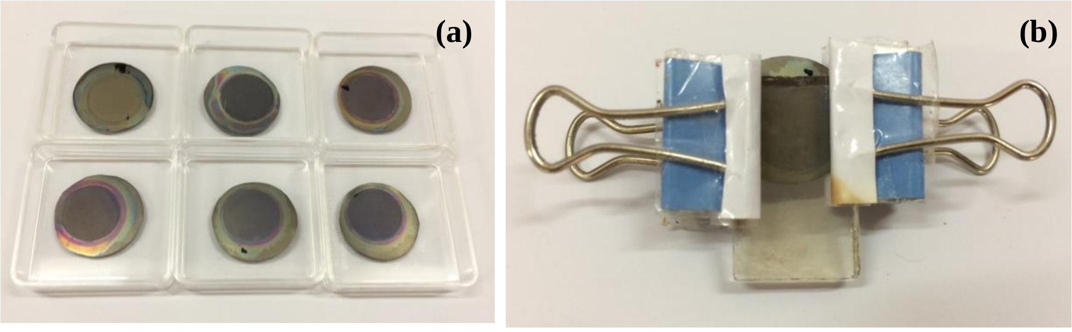

Figure 3.15 (a) Anodized titania nanotube samples with various conditions and (b) Obtained dye-sensitized solar cells (DSSC) device.

3.4 Current-Voltage measurements (I-V)

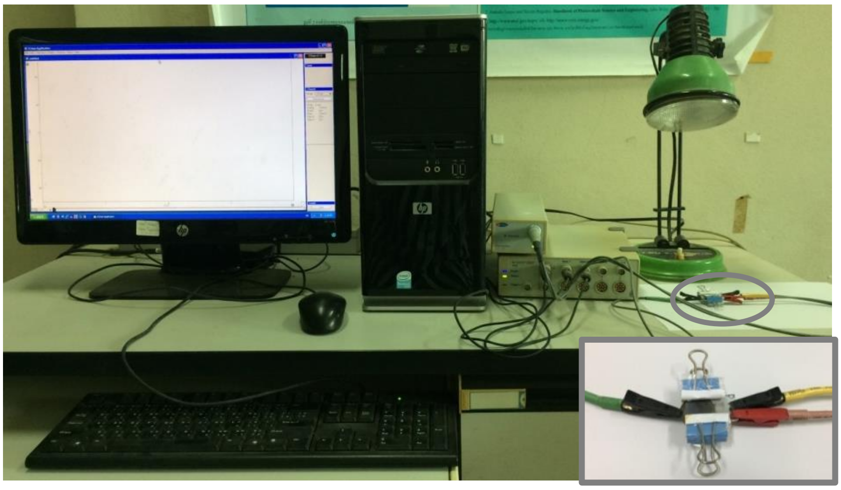

Figure 3.16 The I-V curve measuring instrument for dye-sensitized solar cells.

In DSSCs, It is well known that photo conversion efficiency can be calculated from the current-voltage (I-V) characteristics of dye-sensitized solar cells. The active areas of 0.25 cm^2 of all fabricated samples will be performed by Keithley 2400 source meter as shown in Figure 3.17.

The incident light with intensity of 100 mW/cm^2 from a Xenon arc lamp used as the irradiation source. The overall performance of the DSSCs can be described in terms of the fill factor (FF) and conversion efficiency (η) [88-91] as follows.

$$FF=\frac{V_{mp}\times I_{mp}}{V_{oc}\times I_{sc}} \tag{3.3}$$

$$\eta(\%)=\frac{FF\times V_{oc}\times I_{sc}}{P_{in}}\times 100\% \tag{3.4}$$

where, V_{oc} is open circuit voltage (Volt), I_{sc} is short circuit current density (mA/cm^2), V_{mp} is voltage at maximum power (Volt), is I_{mp} is current at maximum power (mA/cm^2), FF is Fill-factor and P_{in} is incident light power (W) as shown in Figure 3.17.

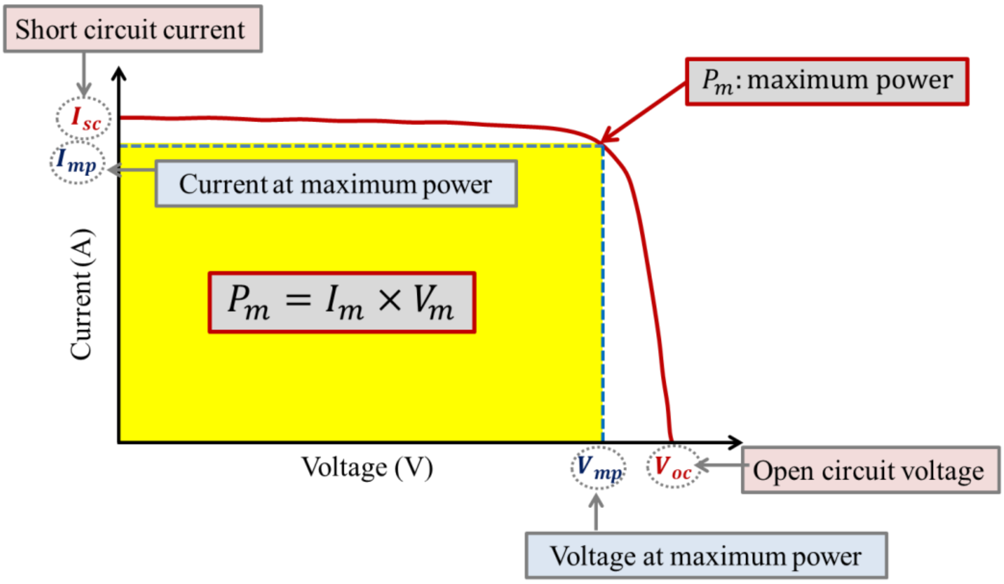

Figure 3.17 Current - Voltage characteristic of dye-sensitized solar cells [74].

CHAPTER 4

RESULTS AND DISCUSSIONS

In this chapter, the results and discussions of the obtained samples will be presented after they were characterized by using X-ray diffraction (XRD), scanning electron microscopy (SEM), UV-visible spectroscopy, atomic force microscopy (AFM), X-ray photoelectron spectroscopy (XPS) and energy dispersive X-ray spectrometer (EDS). The photo conversion efficiency of the photoanodes are also investigated and discussed.

4.1 XRD measurement

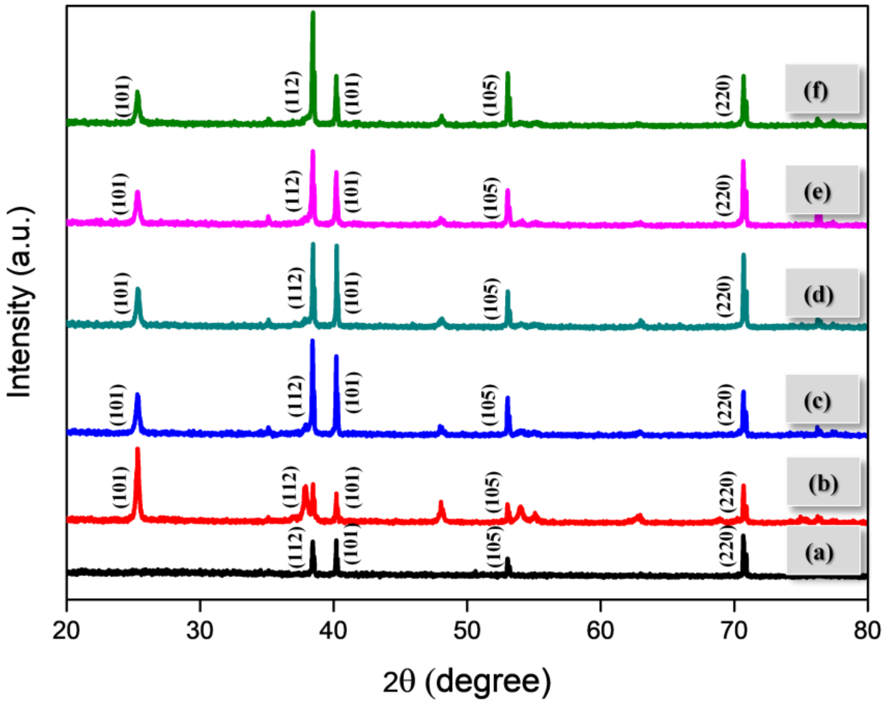

Figure 4.1 XRD patterns of TiO_2 nanotube arrays: (a) as-anodized Ti, (b) annealed TiO_2, (c) annealed 0.05 wt% $K_3[Fe(CN)_6]$-doped TiO_2, (d) annealed 0.10 wt% $K_3[Fe(CN)_6]$-doped TiO_2, (e) annealed 0.15 wt% $K_3[Fe(CN)_6]$-doped TiO_2, and (f) annealed 0.20 wt% $K_3[Fe(CN)_6]$-doped TiO_2.

Figure 4.1 shows the XRD patterns of TiO_2 nanotube arrays: as-anodized Ti (a), annealed TiO_2 (b) and annealed TiO_2 doped with $K_3[Fe(CN)_6]$ at various concentrations (c, d, e, f). It was observed that as-anodized Ti before annealing appeared peaks belong to Ti metal as shown in line (a). For example, four peaks are located at $2\theta = 38.0°$, 40.0°, 57.5°, and 71.0° corresponding to Ti (112), (101), (105), and (220) planes with the interplanar spacings (d) of 0.06, 0.11, 0.07, and 0.03 nm, respectively, derived by hexagonal crystal structure of Ti metal [92]. This XRD pattern indicated that as-anodized sample was amorphous layer on top of Ti metal sheet. Specifically, anatase phase structure of as-anodized Ti (a) was not observed. However, after as-anodized TiO_2 (b) and the TiO_2 were doped with $K_3[Fe(CN)_6]$ and then annealed at 450 °C for 2 h, the XRD peaks suggested phase transformation from amorphous phase to anatase phase occurred. Four peaks located at $2\theta = 25.5°$, 38.0°, 57.5°, and 71.0 ° corresponding to the anatase (101), (112), (105), and (220) planes with the interplanar spacing (d) of 0.35, 0.23, 0.17, and 0.13 nm, respectively. The data was derived by tetragonal crystal structure of TiO_2 that was suitable for the applications in dye-sensitized solar cells [93]. For $K_3[Fe(CN)_6]$ doped titania nanotube samples, the phase of dopants was undetectable by XRD even for highly $K_3[Fe(CN)_6]$ doped samples.

Table 4.1 Lattice parameters of prepared TiO_2 nanotubes.

Samples	**Lattice parameters**			**Volume ($Å^3$)**
	a (Å)	**b (Å)**	**c (Å)**	
Annealed TiO_2 (b)	3.79	3.79	9.51	136.50
Annealed 0.05wt% $K_3[Fe(CN)_6]$-doped TiO_2 (c)	3.78	3.78	9.61	137.16
Annealed 0.10 wt% $K_3[Fe(CN)_6]$-doped TiO_2 (d)	3.78	3.78	9.57	136.54
Annealed 0.15 wt% $K_3[Fe(CN)_6]$-doped TiO_2 (e)	3.78	3.78	9.43	134.36
Annealed 0.20 wt% $K_3[Fe(CN)_6]$-doped TiO_2 (f)	3.77	3.77	9.36	133.45

Moreover, it was found that introducing of $K_3[Fe(CN)_6]$ dopant into the samples had an effect on the lattice parameters of TiO_2 nanotubes. The lattice parameters of TiO_2 nanotubes slightly decreased when the concentrations of the dopant increased as shown in Table 4.1 which leads to decrease of the volume of the unite cells.

4.2 SEM characterization

The detailed surface morphological characterization of as-prepared samples was examined by scanning electron microscopy (SEM) as compared in Figure 4.2. The SEM investigation reveals that the amorphous nanotube region of as-anodized Ti (a) before annealing was not homogenous and appeared less number of nanotubes than pure TiO_2 sample (b) and $K_3[Fe(CN)_6]$ doped TiO_2 nanotube samples (c, d, e, f) after annealing. The diameters of titania nanotube samples were approximately 90 nm, 100 nm, 140 nm, 120 nm, 105 nm, and 120 nm for (a) as-anodized Ti, (b) annealed TiO_2, (c) annealed 0.05 wt% $K_3[Fe(CN)_6]$-doped TiO_2, (d) annealed 0.10 wt% $K_3[Fe(CN)_6]$ doped-TiO_2, (e) annealed 0.15 wt% $K_3[Fe(CN)_6]$-doped TiO_2, and (f) annealed 0.20 wt% $K_3[Fe(CN)_6]$-doped TiO_2, respectively.

Interestingly, the highly ordered nanotube arrangements were found after as-anodized TiO_2 nanotubes were doped with increasing concentrations of $K_3[Fe(CN)_6]$. The effect of the concentration of $K_3[Fe(CN)_6]$ on TiO_2 nanotube arrangement can be described as follows. During the pore formation process, if the formation and dissolution of oxide layer are in an optimum range, highly self-organized oxide pore arrangement or nanotube formation is possible. It is noteworthy that the formation of reaction products also increases the conductivity of the electrolyte and thereby increases the growth rate of the nanotubes [94]. The rate of electron transfer for the ferrocyanide couple on platinum electrodes increases linearly with increasing concentration of added cation. Ferrocyanide solution acts as a buffer during respective formation of the mono, di, tri, and tetra protonated ferricyanide electrolyte [95]. Besides, $K_3[Fe(CN)_6]$ as a buffer solution in the electrolyte can also create the pH gradient which is required for fabricating the nanotubes with longer length. However, increasing the $K_3[Fe(CN)_6]$ concentration in the electrolyte is effective on the pH gradient and yields to the enhancement of the growth rate of nanotubes, respectively[96,97].

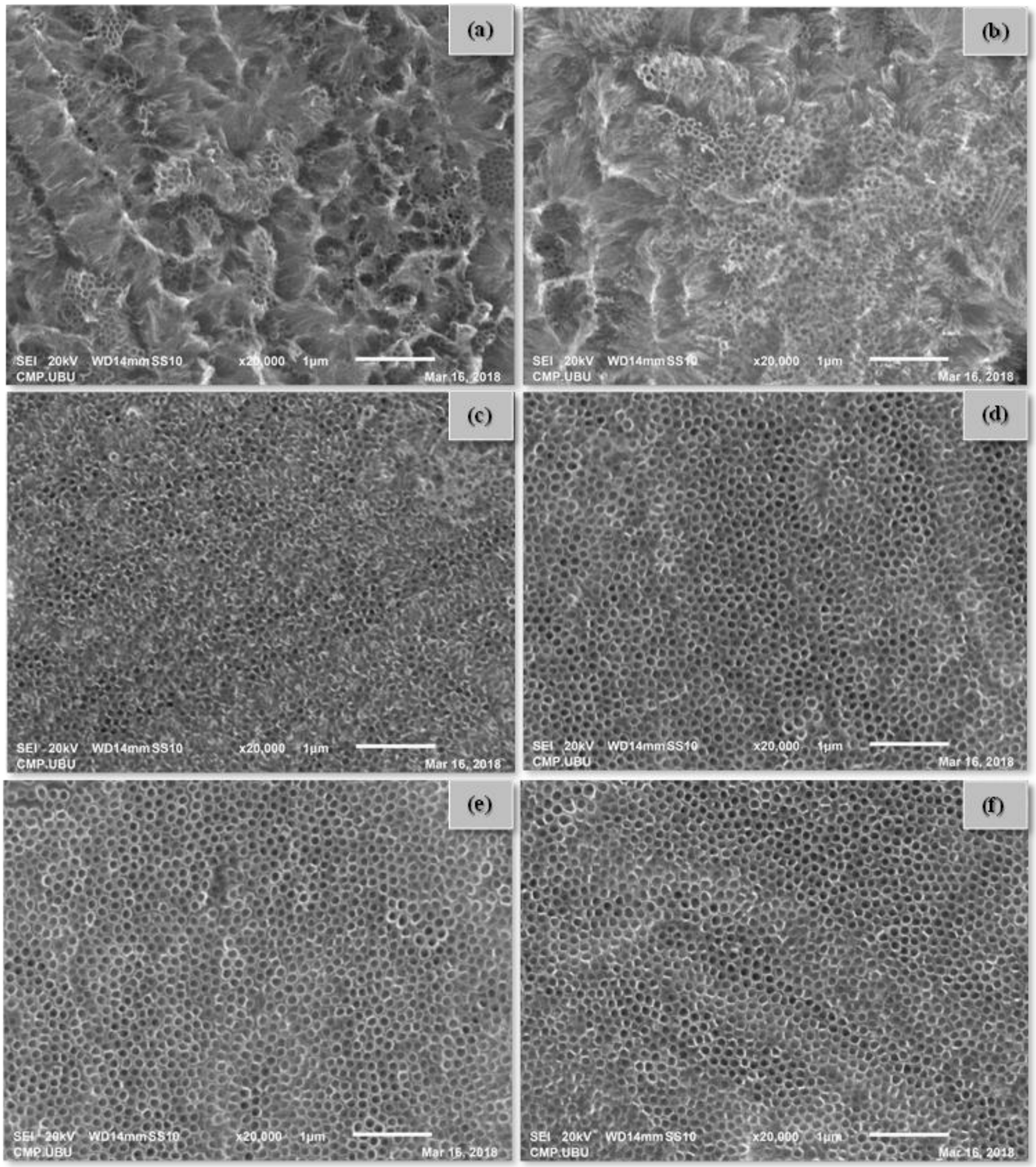

Figure 4.2 **SEM images of TiO_2 nanotube arrays: (a) as-anodized Ti, (b) annealed TiO_2, (c) annealed 0.05 wt% $K_3[Fe(CN)_6]$-doped TiO_2, (d) annealed 0.10 wt% $K_3[Fe(CN)_6]$-doped TiO_2, (e) annealed 0.15 wt% $K_3[Fe(CN)_6]$-doped TiO_2, and (f) annealed 0.20 wt% $K_3[Fe(CN)_6]$-doped TiO_2.**

4.3 UV-visible spectra analysis

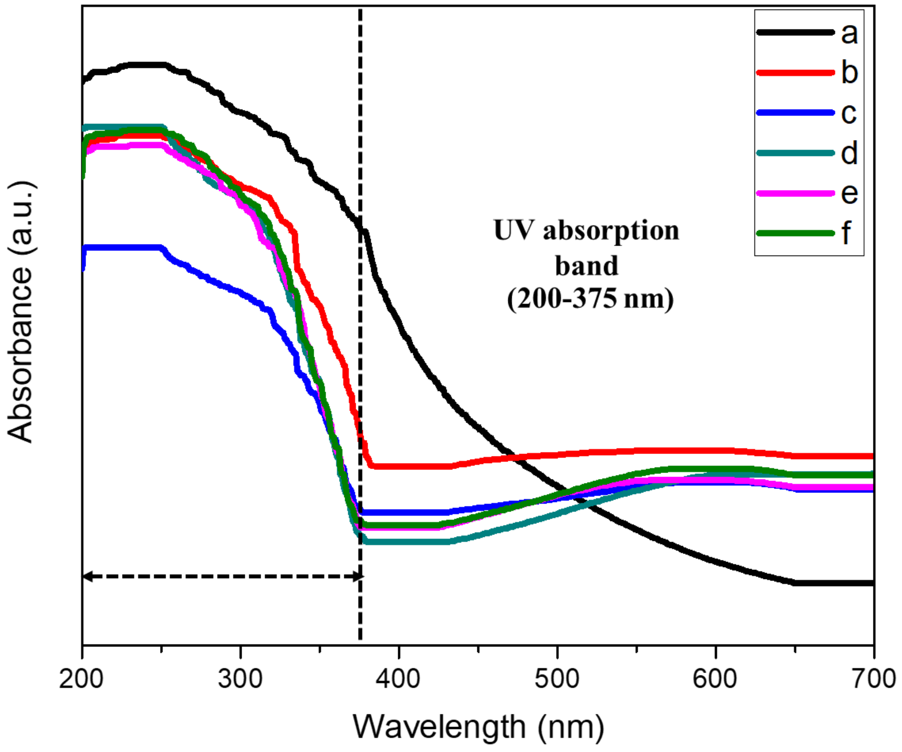

Figure 4.3 Absorbance UV-visible spectra of TiO_2 nanotube arrays: (a) as-anodized Ti, (b) annealed TiO_2, (c) annealed 0.05 wt% $K_3[Fe(CN)_6]$-doped TiO_2, (d) annealed 0.10 wt% $K_3[Fe(CN)_6]$-doped TiO_2, (e) annealed 0.15 wt% $K_3[Fe(CN)_6]$-doped TiO_2, and (f) annealed 0.20 wt% $K_3[Fe(CN)_6]$-doped TiO_2.

Optical properties of samples were effectively characterized by UV-visible (UV-Vis) spectroscopy. The UV-visible absorption spectra of as-anodized Ti sample before annealing (a), pure anodized TiO_2 nanotube sample (b), and various concentrations of $K_3[Fe(CN)_6]$ doped anodized TiO_2 nanotube samples after annealing at 450 °C for 2 h (c, d, e,f) were measured and shown in Figure 4.3. The optical band gap energy of all titania nanotube samples were calculated using a Tauc plot of the modified Kubelka-Munk (MK) function with a linear extrapolation [98-101] as given below.

$$(\alpha h\upsilon)^{1/2} = \beta (h\upsilon - E_g) \qquad (4.1)$$

where, E_g is the Tauc optical band gap, α=2.303A/d (A is optical intensity, and d is thickness of the sample), ν is the frequency of incident light, β is a constant which depends on the width of the localized states in the band gap and h is Planck's constant.

To further investigate the effect of $K_3[Fe(CN)_6]$ dopant on the optical response of TiO_2 nanotube arrays, UV-Vis spectroscopy of all prepared titania nanotube samples were measured. The absorbance of all obtained samples is demonstrated in Figure 4.3. As expected, an intense UV absorption band appeared in rang of 200 to 375 nm in all titania nanotube samples, corresponding to electron- transition from valence band to conduction band.

The comparison of $(\alpha h\upsilon)^{1/2}$ vs. $h\upsilon$ plots are displayed in Figure 4.4 to estimated band gap energy of (a) as-anodized Ti, (b) annealed TiO_2, (c) annealed 0.05 $K_3[Fe(CN)_6]$ doped TiO_2, (d) annealed 0.10 $K_3[Fe(CN)_6]$ doped TiO_2, (e) annealed 0.15 $K_3[Fe(CN)_6]$ doped TiO_2, and (f) annealed 0.20 $K_3[Fe(CN)_6]$ doped TiO_2. The results apparently showed that band gap energy of as-anodized Ti after annealing at 450 °C for 2 h increased from 1.7 eV to 2.3 eV. Moreover, incorporation of $K_3[Fe(CN)_6]$ into TiO_2 nanotubes had effect on band gap energy of TiO_2 nanotube samples that increased from 2.3 eV to 2.9 eV with increasing concentrations of $K_3[Fe(CN)_6]$.

According to Goldschmidt-Pauling rule, by increasing the concentration of transition metal as a dopant can cause an increase in band gap energy. The band gap energy between the valence band and the conduction depends uniquely on the first Fourier coefficient of the crystal potential changes insignificantly with solid size. Therefore, a perturbation to the crystal potential can cause band gap energy to be changed. The ionic radius of Fe^{3+} (0.78 Å) is larger than that of Ti^{4+} (0·74 Å). This result in the bond length of Fe–Ti and Fe–O becomes smaller; in other words, the bond of Fe–Ti and Fe–O contracted. Due to the Goldschmidt-Pauling rule of bond contraction induced by under coordination [102], this result may increase of band gap of titania nanotubes after introducing potassium ferricyanide. Moreover, the increase of band gap is observed as the tube diameter increases [103]. The band gap energy of TiO_2 nanotube samples, after introduced $K_3[Fe(CN)_6]$ with various concentrations, increased from 2.3 eV to 2.5, 2.7, 2.8, and 2.9 eV. In addition, crystallite size of TiO_2 changed from 100 nm to 140,120,105, and 120 nm for 0.05 wt%, 0.10 wt%, 0.15 wt%, and 0.20wt% of $K_3[Fe(CN)_6]$, respectively. From XRD data analysis, the band gap energies of TiO_2 samples were likely to increase when the lattice parameters of TiO_2 samples their slightly increased due to the quantum sized effect [104, 105].

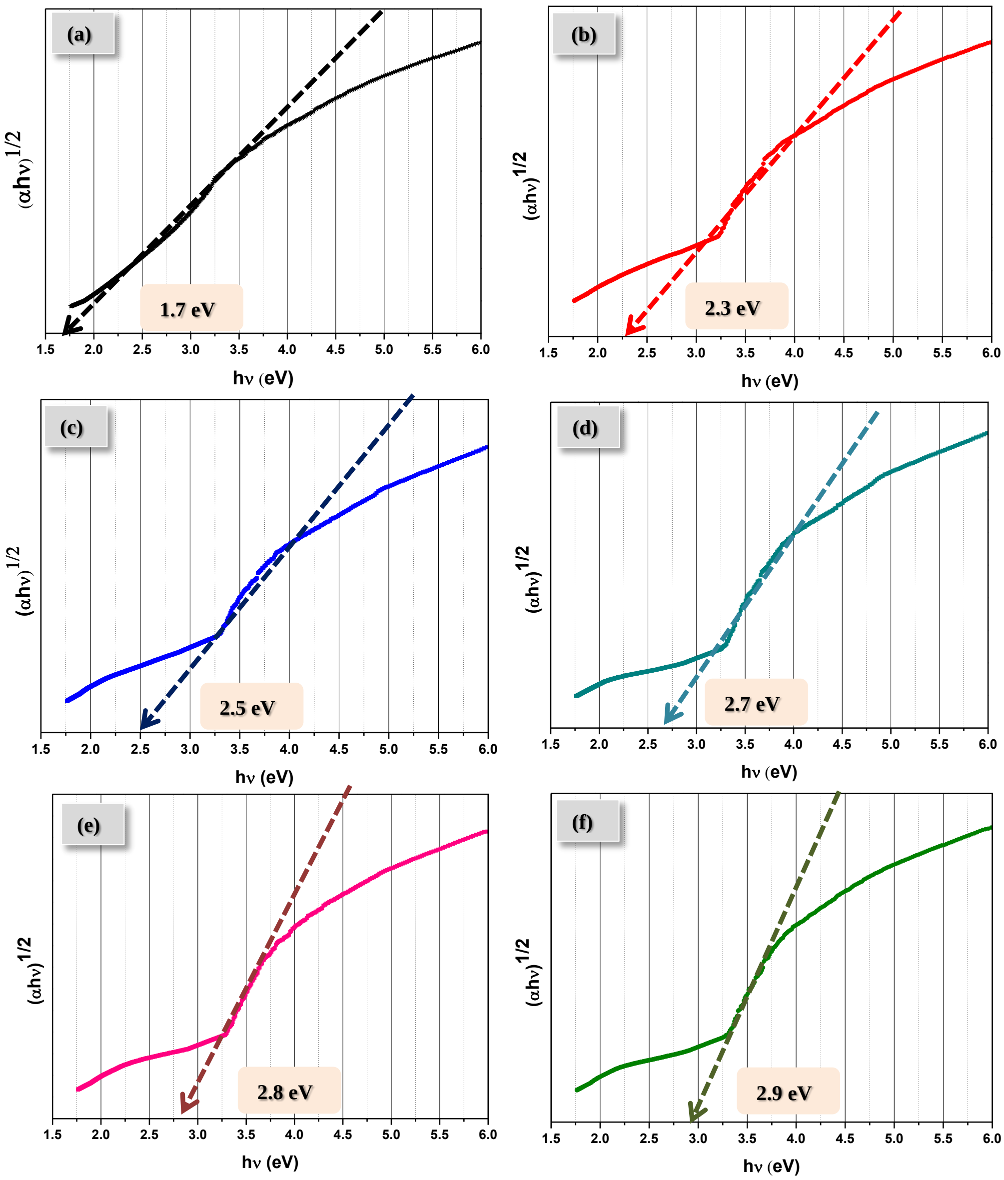

Figure 4.4 Plot of $(\alpha h\upsilon)^{1/2}$ vs. $h\upsilon$ **employed to calculate the band gap value of TiO_2 nanotube arrays: (a) as-anodized Ti, (b) annealed TiO_2, (c) annealed 0.05 wt% $K_3[Fe(CN)_6]$-doped TiO_2, (d) annealed 0.10 wt% $K_3[Fe(CN)_6]$-doped TiO_2, (e) annealed 0.15 wt% $K_3[Fe(CN)_6]$-doped TiO_2, and (f) annealed 0.20 wt% $K_3[Fe(CN)_6]$-doped TiO_2.**

4.4 AFM analysis

The surface morphology of titania nanotube samples was studied by means of Atomic force microscopy (AFM). Two-and three-dimensional AFM images of TiO_2 nanotube arrays: (a) as-anodized Ti before annealing, (b) annealed TiO_2, (c) annealed 0.05 wt% $K_3[Fe(CN)_6]$-doped TiO_2, (d) annealed 0.10 wt% $K_3[Fe(CN)_6]$-doped TiO_2, (e) annealed 0.15 wt% $K_3[Fe(CN)_6]$-doped TiO_2, and (f) annealed 0.20 wt% $K_3[Fe(CN)_6]$-doped TiO_2 after annealing at 450 °C for 2 h are shown in Figure 4.5.

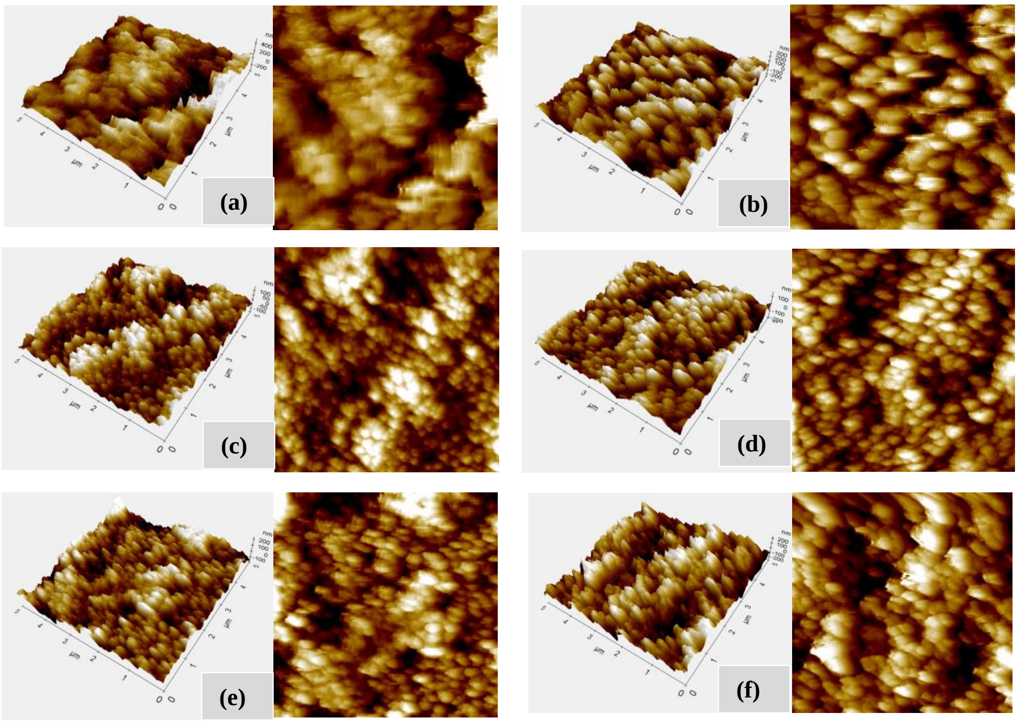

Figure 4.5 Two-and three-dimensional AFM images of TiO_2 nanotube arrays: (a) as-anodized Ti, (b) annealed TiO_2, (c) annealed 0.05 wt% $K_3[Fe(CN)_6]$-doped TiO_2, (d) annealed 0.10 wt% $K_3[Fe(CN)_6]$-doped TiO_2, (e) annealed 0.15 wt% $K_3[Fe(CN)_6]$-doped TiO_2, and (f) annealed 0.20 wt% $K_3[Fe(CN)_6]$-doped TiO_2.

From AFM data analysis, different conditions of anodization yielded different surface morphology of roughness. Table 4.2 shows three surface roughness parameters: the root mean square roughness (R_q), ratio of peak to valley (R_{p-v}), and average roughness (R_{ave}) [106] of the samples. It is significant to notice that the average roughness can be the same for two surfaces, while their roughness profiles were completely different. The three parameters of titania nanotube samples generally decreased by increasing concentrations of $K_3[Fe(CN)_6]$ after annealing. The reduction of ratio of peak to valley (R_{p-v}) after doping of $K_3[Fe(CN)_6]$ on titania nanotube samples means that the surface were smoother. This may give initial evidence that there was the reduction in the surface to volume ratio after introducing $K_3[Fe(CN)_6]$ into titania nanotubes.

Table 4.2 Surface roughness parameters values from AFM measurement for titania nanotube samples.

Samples	**R_{p-v} (nm)**	**R_q (nm)**	**R_{ave} (nm)**
As-anodized Ti (a)	903.661	97.960	74.942
Annealed TiO_2 (b)	575.238	71.130	56.866
Annealed 0.05wt% $K_3[Fe(CN)_6]$-doped TiO_2 (c)	434.774	48.093	38.001
Annealed 0.10 wt% $K_3[Fe(CN)_6]$-doped TiO_2 (d)	361.202	48.289	37.715
Annealed 0.15 wt% $K_3[Fe(CN)_6]$-doped TiO_2 (e)	290.625	46.389	37.413
Annealed 0.20 wt% $K_3[Fe(CN)_6]$-doped TiO_2 (f)	276.383	41.139	33.271

4.5 XPS analysis

The chemical states of the prepared samples were characterized by XPS as shown in Figure 4.6. Overall XPS spectra of all prepared samples appeared peaks of Ti 2p, O 1s, and C 1s while the peaks of Fe and N were not observed in the XPS spectrum for $K_3[Fe(CN)_6]$ doped titania nanotube samples. Two peaks of Ti 2p XPS spectra of all prepared samples were observed. Ti $2p_{3/2}$ at approximately 458.64 eV and Ti $2p_{1/2}$ at approximately 464.35 eV were assigned to the Ti-O metal oxide bonding [107, 108]. The distance between them was approximately 5.71 eV which confirmed that the main chemical state of Ti in TiO_2 anotube lattices is Ti^{4+} [109]. Moreover, it was found that the introduction of $K_3[Fe(CN)_6]$ at concentration of 0.20 wt% had an effect on binding energy of Ti 2p that shifted towards lower binding energy from 458.64 eV and 464.35 eV to 457.69 eV and 463.39 eV for Ti $2p_{3/2}$ and Ti $2p_{1/2}$, respectively as compared in Figure 4.7. The energy shift happened to all titania nanotube samples which suggested that this could be the result of reduction of Ti^{4+} to Ti^{3+}. Accordingly, the negative charge introduced in the lattice of nanotubes is instead compensated by conversion of Ti^{4+} to Ti^{3+}. This conversion utilized the charge transfer between anions and cations due to the higher percentage of loosely bound Ti^{3+} - O bonds compared with the stronger Ti^{4+} -O bonds. Consequently, the electrochemical performance of titania nanotubes was enhanced. Further, this less oxidized Ti^{3+} states indicated higher oxygen deficiencies within the titania nanotubes [110-111]. The O 1s XPS spectra of all prepared samples at approximately 529.87 eV was assigned to the O - Ti bonding [112]. The C 1s X spectra of all prepared samples at approximately 284.9 eV was assigned, due to carbon absorption on the surface as pollutant (C–C bonds) [113].

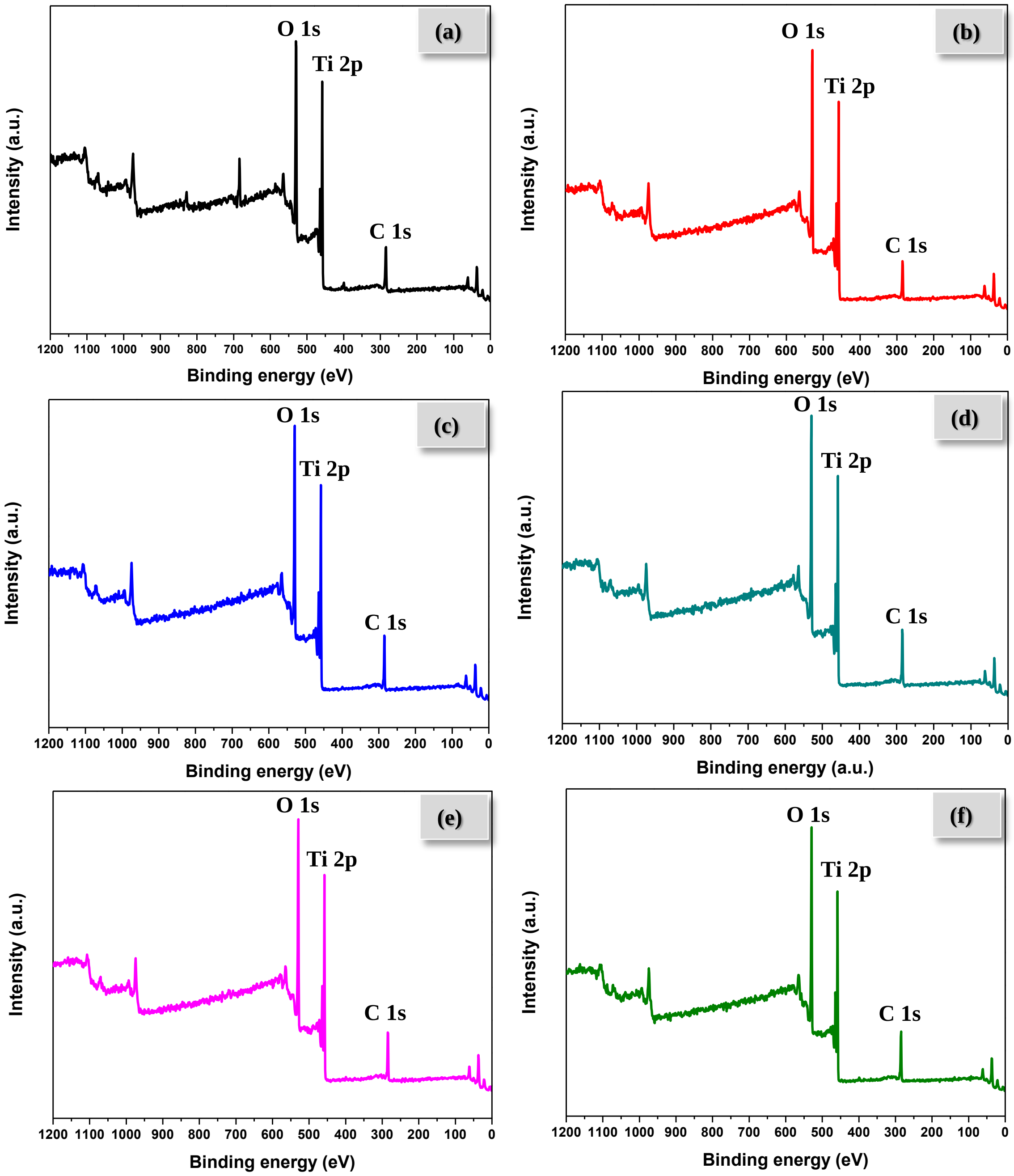

Figure 4.6 **Over all XPS spectra of TiO_2 nanotube arrays: (a) as-anodized Ti, (b) annealed TiO_2, (c) annealed 0.05 wt% $K_3[Fe(CN)_6]$-doped TiO_2, (d) annealed 0.10 wt% $K_3[Fe(CN)_6]$- doped TiO_2, (e) annealed 0.15 wt% $K_3[Fe(CN)_6]$-doped TiO_2, and (f) annealed 0.20 wt% $K_3[Fe(CN)_6]$-doped TiO_2.**

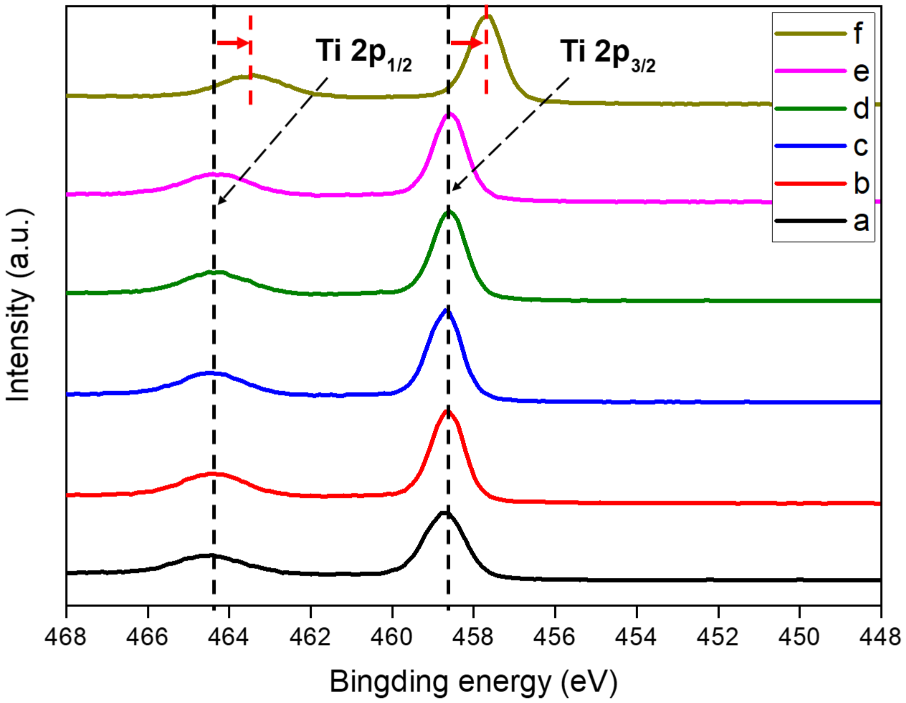

Figure 4.7 The comparison of Ti 2p line shapes of TiO_2 nanotube arrays: (a) as-anodized Ti, (b) annealed TiO_2, (c) annealed 0.05 wt% $K_3[Fe(CN)_6]$-doped TiO_2, (d) annealed 0.10 wt% $K_3[Fe(CN)_6]$-doped TiO_2, (e) annealed 0.15 wt% $K_3[Fe(CN)_6]$-doped TiO_2, and (f) annealed 0.20 wt% $K_3[Fe(CN)_6]$-doped TiO_2.

4.6 EDS analysis

The EDS spectra and chemical compositions of titania nanotube samples are compared in Figure 4.8 and Table 4.3, respectively. It was found that all the nanotube-formed surfaces were composed of Ti, O, and C. Note that C in EDS result is attributed to the conductive carbon adhesive during the EDS test. Although Fe and N were not detected for the $K_3[Fe(CN)_6]$ doped samples, after $K_3[Fe(CN)_6]$ at various concentrations was doped, amount of Ti slightly increased while amount of O negligibly decrease in all doped samples. This result may inferred that $K_3[Fe(CN)_6]$ supported the formation of TiO_2 nanotubes which in accordance with the SEM results.

Table 4.3 EDS compositions of anodized samples.

Samples	**Weight %**				**Atomic %**			
	Ti	**O**	**C**	**Total**	**Ti**	**O**	**C**	**Total**
As-anodized Ti (a)	47.14	45.55	7.31	100	22.17	64.13	13.70	100
Annealed TiO_2 (b)	48.85	44.90	6.26	100	23.24	64.56	11.98	100
Annealed 0.05wt% $K_3[Fe(CN)_6]$-doped TiO_2 (c)	53.72	40.78	5.49	100	27.17	61.75	11.08	100
Annealed 0.10 wt% $K_3[Fe(CN)_6]$-doped TiO_2 (d)	53.10	41.24	5.66	100	26.66	61.99	11.34	100
Annealed 0.15 wt% $K_3[Fe(CN)_6]$-doped TiO_2 (e)	53.72	40.78	5.49	100	27.17	61.75	11.08	100
Annealed 0.20wt% $K_3[Fe(CN)_6]$-doped TiO_2 (f)	53.20	40.93	5.87	100	26.72	61.53	11.75	100

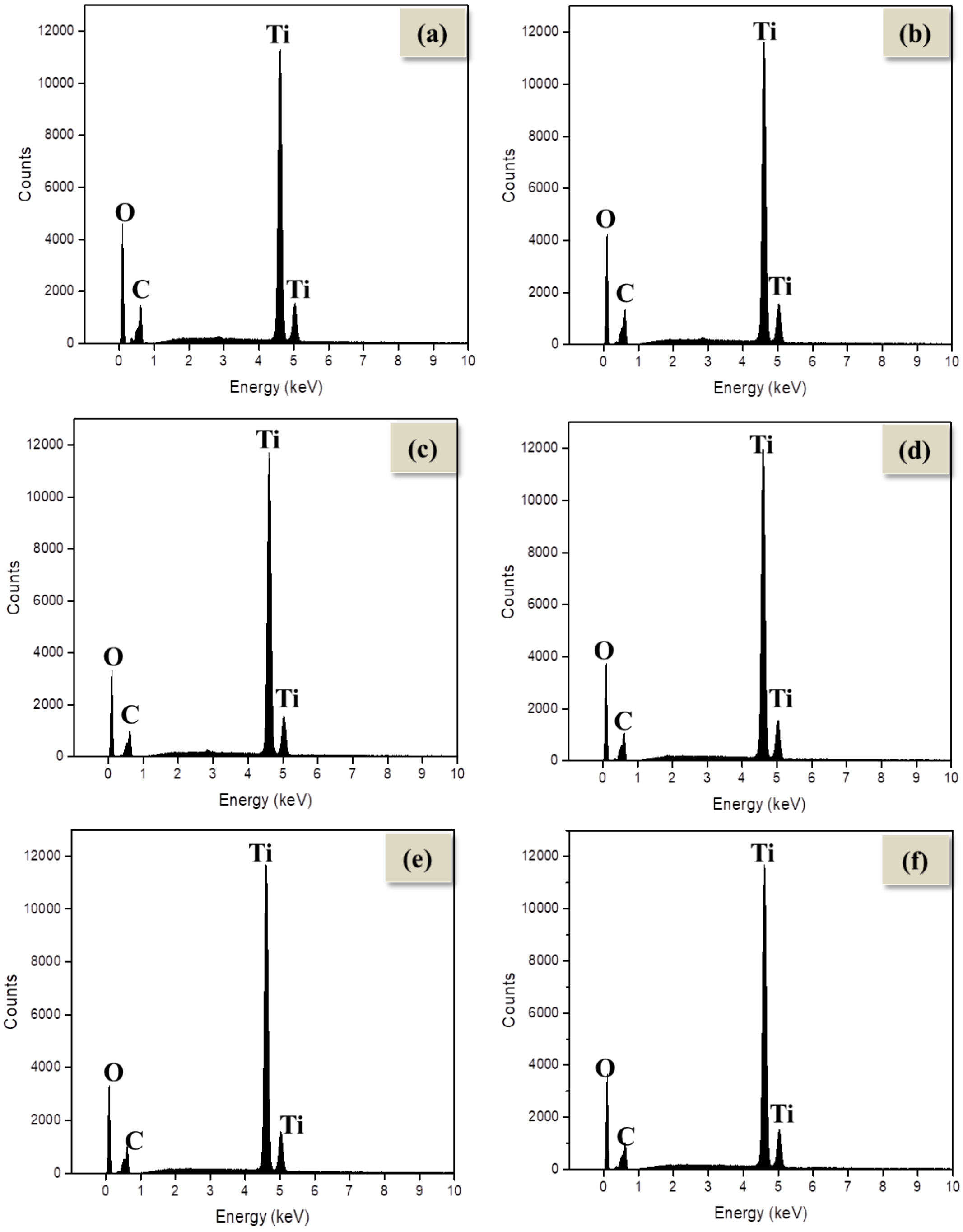

Figure 4.8 EDS peaks of TiO_2 nanotube arrays: (a) as-anodized Ti, (b) annealed TiO_2, (c) annealed 0.05 wt% $K_3[Fe(CN)_6]$-doped TiO_2, (d) annealed 0.10 wt% $K_3[Fe(CN)_6]$-doped TiO_2, (e) annealed 0.15 wt% $K_3[Fe(CN)_6]$-doped TiO_2, and (f) annealed 0.20 wt% $K_3[Fe(CN)_6]$-doped TiO_2.

4.7 Photovotaic performance of dye-sensitized solar cells

In addition, the DSSCs with photoanodes were investigated for their performance in DSSCs by measuring the current-voltage behavior under illumination with 100 mW/cm^2 light intensity. The photocurrent density- photovoltage (I-V) curves for dye-sensitized solar cells on TiO_2 nanotube arrays: (a) as-anodized Ti, (b) annealed TiO_2, (c) annealed 0.05 wt% $K_3[Fe(CN)_6]$-doped TiO_2, (d) annealed 0.10 wt% $K_3[Fe(CN)_6]$-doped TiO_2, (e) annealed 0.15 wt% $K_3[Fe(CN)_6]$-doped TiO_2, and (f) annealed 0.20 wt% $K_3[Fe(CN)_6]$-doped TiO_2 are presented in Figure 4.9 and their solar cell parameters are evaluated and displayed in Table 4.4.

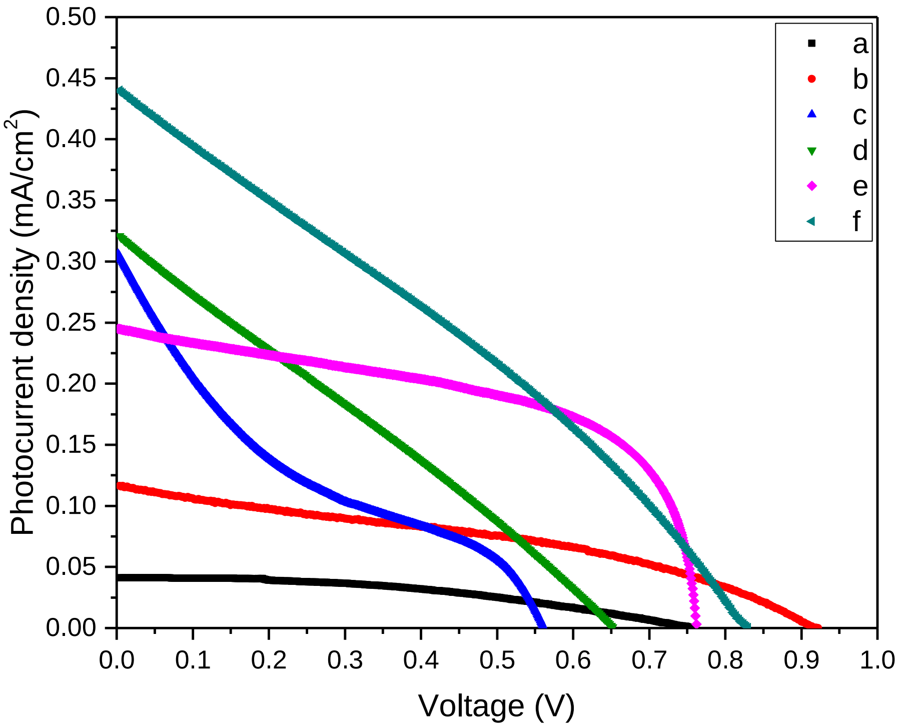

Figure 4.9 I-V characteristics of fabricated DSSCs on TiO_2 nanotube arrays: (a) as-anodized Ti, (b) annealed TiO_2, (c) annealed 0.05 wt% $K_3[Fe(CN)_6]$-doped TiO_2, (d) annealed 0.10 wt% $K_3[Fe(CN)_6]$-doped TiO_2, (e) annealed 0.15 wt% $K_3[Fe(CN)_6]$-doped TiO_2, and (f) annealed 0.20 wt% $K_3[Fe(CN)_6]$-doped TiO_2.

Table 4.4 Photovoltaic parameters of fabricated DSSCs with different photoanode samples.

Samples	**V_{mpp} (V)**	**I_{mpp} (mA)**	**V_{oc} (V)**	**I_{sc} (mA)**	**Efficiency (%)**
As-anodized Ti (a)	0.434	0.029	0.758	0.041	0.021
Annealed TiO_2 (b)	0.614	0.064	0.922	0.116	0.066
Annealed 0.05 wt% $K_3[Fe(CN)_6]$-doped TiO_2 (c)	0.411	0.081	0.561	0.306	0.055
Annealed 0.10 wt% $K_3[Fe(CN)_6]$-doped TiO_2 (d)	0.354	0.158	0.652	0.320	0.093
Annealed 0.15wt% $K_3[Fe(CN)_6]$-doped TiO_2 (e)	0.613	0.169	0.762	0.244	0.173
Annealed 0.20 wt% $K_3[Fe(CN)_6]$-doped TiO_2 (f)	0.474	0.228	0.830	0.440	0.180

The results apparently show that the solar cell efficiencies of fabricated DSSCs of as-anodized Ti after annealing at 450 °C for 2 h increased from 0.021% to 0.066%. Moreover, incorporation of $K_3[Fe(CN)_6]$ into TiO_2 nanotubes had effect on the solar cell efficiencies of annealed TiO_2 nanotube samples that increased from 0.066 % to 0.180% with increasing concentrations of $K_3[Fe(CN)_6]$. Interestingly, TiO_2 nanotube sample after introduced with $K_3[Fe(CN)_6]$ at concentration of 0.20 wt% exhibited highest solar cell efficiency than other samples in this work. This result may inferred that after introducing $K_3[Fe(CN)_6]$ at concentration of 0.20% in ethylene glycol based anodizing electrolyte enhanced the electrochemical performance of TiO_2 nanotubes which in accordance with the XPS result.

From theoretical point of view, the decrease of lattice parameters of the sample results in increase of the band gap energy. Thus, the conversion efficiency of the samples should decrease because of the quantum size effect [104-105]. However, from the experimental data, the efficiency of the DSSC increased. This result can be explained as follows. Accordance with SEM data, highly ordered, vertically oriented

TiO_2 nanotube-arrays offers a large internal surface area without a concomitant decrease in geometric and structural order. The precisely oriented nature of the nanotube array makes them excellent electron percolation pathways for charge transfer between interfaces [75] lead to exhibited highest DSSC efficiency. Accordance with XRD data analysis, the anatase phase structure of TiO_2 nanotube samples plays a key role in the injection process of photochemical solar cells with high conversion efficiency and appears to have a wider optical absorption gap and a smaller electron effective mass, resulting in a higher mobility for the charge carriers. Good crystallinity is required for smooth electron flow in the nanotubes for the efficient dye-sensitized solar cell [72].

CHAPTER 5

CONCLUSION AND RECOMMENDATION

5.1 Conclusion

This work reports the effect of $K_3[Fe(CN)_6]$ on the performance of TiO_2 nanotubes. Highly ordered TiO_2 nanotubes were successfully fabricated via one-faced and single-step anodizing technique with voltage at 50 V for 2 h in ethylene glycol based electrolytes consisting of 0.25 wt% NH_4F and 2 vol% DI-water (H_2O), while the concentrations of $K_3[Fe(CN)_6]$ were varied from 0.05 wt% to 0.20 wt% with increment of 0.05 wt%. After that, the specimens were annealed at 450 °C for 2 h to obtain anatase phase structures. The obtained samples were characterized by using XRD, SEM, AFM, XPS, EDS and UV-visible spectrophotometer. The different specimens were used as photoanodes and assembled to DSSCs as described in the experimental section. The results of sample characterizations and photovoltaic performances of them in DSSCs can be summarized as follows:

XRD analysis confirmed that the crystalline nature of all samples after annealing at 450 °C for 2 h was anatase crystalline phase structures. As-anodized Ti before calcination appeared peaks belong to Ti metal. However, anatase phase structure of as-anodized Ti was not observed. In contrast, after TiO_2 were doped with $K_3[Fe(CN)_6]$ at various concentrations and annealed at 450 °C for 2 h, the XRD peaks suggested phase transformation from amorphous phase to anatase phase which are suitable for the applications in dye- sensitized solar cells.

SEM images revealed the nanotube structures of synthesized products. Interestingly, the highly ordered nanotube arrangements were found after as-anodized TiO_2 nanotubes were introduced with increasing the concentrations of $K_3[Fe(CN)_6]$. The diameters of titania nanotube samples were approximately 90 nm-140 nm.

Optical properties of the obtained samples which were characterized by UV-visible spectroscopy shown that all titania nanotube samples appeared an intense UV absorption band in rang of 200 to 375 nm, corresponding to electron- transition from valence band to conduction band. Moreover, the results apparently demonstrated that band gap energy of as-anodized Ti after annealing at 450 °C for 2 h increased from 1.7 eV to 2.3 eV and incorporation of $K_3[Fe(CN)_6]$ into TiO_2 nanotubes had effect on band gap energy of TiO_2 nanotube samples that increased from 2.3 eV to 2.9 eV with increasing concentrations of $K_3[Fe(CN)_6]$.

AFM measurement reported that the three surface roughness parameter values of TiO_2 nanotubes decreased with increasing concentrations of $K_3[Fe(CN)_6]$, which made the surface of TiO_2 nanotubes were smoother.

XPS data revealed that all titania nanotube samples composed of Ti and O. Although Fe and N were not detected in XPS measurement, doping of $K_3[Fe(CN)_6]$ at concentration of 0.20 wt% caused Ti 2p shifted towards lower binding energy. This could be a result of reduction of Ti^{4+} to Ti^{3+}, thus improving the photocatalytic reaction of titania nanotubes.

EDS analysis found that all the nanotube-formed surfaces were composed of Ti, O, and C. Although Fe and N were not detected for the $K_3[Fe(CN)_6]$ doped samples, after $K_3[Fe(CN)_6]$ at various concentrations was doped, amount of Ti slightly increased while amount of O negligibly decrease in all doped samples.

The result of photovoltaic performances in DSSCs found that the fabricated 0.20wt% of $K_3[Fe(CN)_6]$ doped TiO_2 nanotubes which was used as photoanode in DSSC exhibited highest solar cell efficiency than other samples. This work suggests an alternative method for fine tuning the size of TiO_2 nanotube arrays that widely applied in the field energy conversion materials for DSSCs.

5.2 Recommendation

For future development of this work and the improvement of titania nanotube performance, it is recommended to investigate the influence of $K_3[Fe(CN)_6]$ with more various concentrations which are greater than 0.20wt% with increment of 0.05wt%. It may be found alternative method for fine tuning the size of TiO_2 nanotube arrays and lead to the better discovery of the suitable way to develop photovoltaic performance of TiO_2 nanotubes as photoanodes in DSSCs. In addition, TiO_2 nanotubes after introducing with 0.20wt% $K_3[Fe(CN)_6]$ may be developed and applied into other energy conversion applications such as working electrodes for hydrogen production by photoelectrocatalytic water splitting.

REFERENCES

REFERENCES

[1] Amir Shahsavari and Morteza Akbari. "Potential of solar energy in developing countries for reducing energy-related emissions", **Renewable and Sustainable Energy Reviews**. 90: 275-291; July, 2018.

[2] Dorota Chwieduk. "Impact of solar energy on the energy balance of attic rooms in high latitude countries", **Applied Thermal Engineering**. 136: 548-559; 25 May, 2018.

[3] S. Shalinia and et al. "Review on natural dye sensitized solar cells: Operation, materials and methods", **Renewable and Sustainable Energy Reviews**. 51: 1306-1325; November, 2015.

[4] M. RitaNarayan. "Review: Dye sensitized solar cells based on natural photosensitizers", **Renewable and Sustainable Energy**. 16(1): 208-215; January, 2012.

[5] Michael Grätzel. "Dye-sensitized solar cells", **Journal of Photochemistry and Photobiology C: Photochemistry Reviews**. 4(2): 145-153; 31 October, 2003.

[6] Jiawei Gong and et al. "Review on dye-sensitized solar cells (DSSCs): Advanced techniques and research trends", **Renewable and Sustainable Energy Reviews**. 68(1): 234-246; February, 2017.

[7] Jiawei Gonga, Jing Liangb and K.Sumathy. "Review on dye-sensitized solar cells (DSSCs): Fundamental concepts and novel materials", **Renewable and Sustainable Energy Reviews.** 16(8): 5848-5860; October, 2012.

[8] M. Fitra and et al. "TiO_2 Dye Sensitized Solar Cells Cathode Using Recycle Battery", **Energy Procedia**. 36: 333-340, 2013.

[9] F.I.M. Fazlia and et al. "Dye-sensitized solar Cell using pure anatase TiO_2 annealed at different temperatures", **Optik**. 140: 1063-1068; July, 2017.

[10] Diah Susanti and et al. "The Preparation of Dye Sensitized Solar Cell (DSSC) from TiO_2 and Tamarillo Extract", **Procedia Chemistry**. 9: 3-10, 2014.

[11] Takeo OKU and et al. "Fabrication and characterization of TiO_2-based dye-sensitized solar cells", **Progress in Natural Science: Materials International**. 21(2): 122-126; April, 2011.

REFERENCES (CONTINUED)

[12] U. Opara Krašovec and et al. "Unique TiO_2 paste for high efficiency dye-sensitized solar cells", **Solar Energy Materials and Solar Cells**. 93(3): 379-381; March, 2009.

[13] Judy N.Hart and et al. "TiO_2 sol–gel blocking layers for dye-sensitized solar cells", **Comptes Rendus Chimie**. 9(5–6): 622-626; May–June, 2006.

[14] T. Plirdpring and et al. "Preparation and surface wettability of nanostructure TiO_2 films", **Materials Today: Proceedings**. 4(5): 6331-6335, 2017.

[15] Qinghua Chen and et al. "TiO_2 nanobelts – Effect of calcination temperature on optical, photoelectrochemical and photocatalytic properties", **Electrochimica Acta**. 111: 284-291; 30 November, 2013.

[16] Jun Du and et al. "Self-induced preparation of TiO_2 nanowires by chemical vapor deposition", **Journal of Crystal Growth**. 427: 54-59; October, 2015.

[17] M.M.Viana, V.F.Soares and N.D.S. Mohallem. "Synthesis and characterization of TiO_2 nanoparticles", **Ceramics International**. 36(7): 2047-2053; September, 2010.

[18] Jing Ma and et al. "Growth of TiO_2 nanoflowers photoanode for dye-sensitized solar cells", **Journal of Alloys and Compounds**. 692: 1004-1009; January, 2017.

[19] Fei Huang and et al. "Self-assembled synthesis of TiO_2/TiB_2 nanowall and its photocatalytic properties", **Journal of Alloys and Compounds.** 574: 49-5315; October, 2013.

[20] Seung-Min Oh and Takamasa Ishigaki. "Preparation of pure rutile and anatase TiO_2 nanopowders using RF thermal plasma", **Thin Solid Films**. 457(1): 186-191; 1 June, 2004.

[21] Riyanto Edy and et al. "TiO_2 nanosheets synthesized by atomic layer deposition for photocatalysis", **Progress in Natural Science: Materials International**. 26(5): 493-497; October, 2016.

[22] Mikk Vahtrus and et al. "Mechanical characterization of TiO_2 nanofibers produced by different electrospinning techniques", **Materials Characterization**. 100: 98-103; February, 2015.

REFERENCES (CONTINUED)

[23] Qiaozhen Yu, Mang Wang and Hongzheng Chen. “Fabrication of ordered TiO_2 nanoribbon arrays by electrospinning”, **Materials Letters**. 64(3): 428-430; 15 February, 2010.

[24] Mahdi Kazazi, Pedram Abdollahi, and MahdiMirzaei-Moghadam. “High surface area TiO_2 nanospheres as a high-rate anode material for aqueous aluminium-ion batteries”, **Solid State Ionics**. 300: 32-37; February, 2017.

[25] Gang Cheng and Florian J.Stadler. “Facile synthesis and characterization of TiO_2 nanodots and TiO_2 nanodots@MWCNTs composite via solvothermal method”, **Materials Letters**. 113: 71-75; 15 December, 2013.

[26] Yan Zhou, En-Yong Ding, and Wei-Dong. “Synthesis of TiO_2 nanocubes induced by cellulose nanocrystal (CNC) at low temperature”, **Materials Letters**. 61(28): 5050–5052; November, 2007.

[27] K.T.Park and et al. “Nanoclusters of TiO_2 wetted with gold”, **Surface Science**. 603(20): 3131-3135; 15 October, 2009.

[28] Dong Zhong and et al. “Synthesis of oriented TiO_2 nanocones with fast charge transfer for perovskite solar cells”, **Nano Energy**. 11: 409-418; January, 2015.

[29] Cédric B.D.Marien and et al. “TiO_2 Nanotube arrays: Influence of tube length on the photocatalytic degradation of Paraquat”, **Applied Catalysis B: Environmental**. 194: 1-6; 5 October, 2016.

[30] Bipul Sarkar and et al. “Morphology-controlled synthesis of TiO_2 nanostructures for environmental application”, **Catalysis Communications**. 74: 43–48; 10 January, 2016.

[31] A.Pal, T.K.Jana and K.Chatterjee. “Silica supported TiO_2 nanostructures for highly efficient photocatalytic application under visible light irradiation”, **Materials Research Bulletin**. 76: 353-357; April, 2016.

[32] Mehul Bhogaita and et al. “Synthesis characterization of TiO_2 thin films for DSSC prototype”, **materialstoday: PROCEEDING**. 3(6): 2052–2061; 2016.

REFERENCES (CONTINUED)

[33] Mehul Bhogaita and et al. “Highly selective one-dimensional TiO_2-based nanostructures for air treatment applications”, **Materials Today: Proceedings.** 3(6): 2052-2061, 2016.

[34] Timur Sh.Atabaev and et al. “Pt-coated TiO_2 nanorods for photoelectrochemical water splitting applications”, **Results in Physics**. 6: 373-376, 2016.

[35] S. Ananth and et al. “Direct synthesis of natural dye mixed titanium dioxide nano particles by sol–gel method for dye sensitized solar cell applications”, **Optik**. 125(1): 495-498; January, 2014.

[36] Saeid Zanganeh and et al. “Hydrothermal synthesis and characterization of TiO_2 nanostructures using LiOH as a solvent”, **Advanced Powder Technology**. 22(3): 336-339; May, 2011.

[37] S.Y. Kim, J.H. Yu and J.S. Lee. “The characteristics of nanosized TiO_2 powders synthesized by chemical vapor condensation”, **Nanostructured Materials**. 12(1–4): 471-474, 1999.

[38] Zhongwei Liu and et al. “Production of titanium dioxide powders by atmospheric pressure plasma jet”, **Physics Procedia**. 18: 168-173, 2011.

[39] Sineenart Suphankij, Wanichay Mekprasart and Wisanu Pecharapa. “Photocatalytic of N-doped TiO_2 Nanofibers Prepared by Electrospinning”, **Energy Procedia.** 34: 751-756, 2013.

[40] Peep Uudeküll and et al. “Atomic layer deposition of titanium oxide films on As-synthesized magnetic Ni particles: Magnetic and safety properties”, **Journal of Magnetism and Magnetic Materials.** 429: 299-304; 1 May, 2017.

[41] Xuemei Zhou and et al. “Anodic TiO_2 nanotube layers: Why does self-organized growth occur—A mini review”, **Electrochemistry Communications**. 46: 157-162; September, 2014.

[42] Guo-jian CAO and et al. “Fabrication and photodegradation properties of TiO_2 nanotubes on porous Ti by anodization”, **Transactions of Nonferrous Metals Society of China.** 24(8): 2581-2587; August, 2014.

REFERENCES (CONTINUED)

[43] Alireza Sasani and et al. “Structural and electronic properties of Mg and Mg-Nb co-doped TiO_2 (101) anatase surface”, **Applied Surface Science**. 384: 298-303; 30 October, 2016.

[44] Dahyunir Dahlan and et al. “Synthesis of two-dimensional nanowall of Cu-Doped TiO_2 and its application as photoanode in DSSCs”, **Physica E: Low-dimensional Systems and Nanostructures**. 91: 185-189; July, 2017.

[45] Mohamed S.Mahmoud and et al. “Demonstrated photons to electron activity of S-doped TiO_2 nanofibers as photoanode in the DSSC”, **Materials Letters**. 225: 77-81; 15 August, 2018.

[46] Burak Ünlü, Soner Çakar and Mahmut Özacar. “The effects of metal doped TiO_2 and dithizone-metal complexes on DSSCs performance”, **Solar Energy**. 166: 441-449; 15 May, 2018.

[47] S Shalini and et al. “Studies on DSSC encompassing flower shaped assembly of Na-doped TiO_2 nanorods sensitized with extract from petals of Kigelia Africana”, **Optik**. 155: 334-343; February, 2018.

[48] A.K.Pandey and et al. “Improved electron density through hetero-junction binary sensitized TiO_2/ CdTe / D719 system as photoanode for dye sensitized solar cell”, **Physica E: Low-dimensional Systems and Nanostructures**. 101: 139-143; July, 2018.

[49] M.M.Momeni and et al. “Silver nanoparticles decorated titanium dioxide-tungsten trioxide nanotube films with enhanced visible light photo catalytic activity”, **Ceramics International**. 43: 564-570; January, 2017.

[50] X. Zhou and et al. “Preparation of B, N-codoped nanotube arrays and their enhanced visible light photoelectrochemical performances”, **Electrochemistry Communications**. 13: 121-124; February, 2011.

[51] Q. Wang and et al. “Solvothermal preparation of Fe-doped TiO_2 nanotube arrays for enhancement in visible light induced photoelectrochemical performance”, **Journal of Alloys and Compounds**. 690: 139-144; January, 2017.

REFERENCES (CONTINUED)

[52] Dharmasena Peramunage and Stuart Licht. “Ligand, cation and speciation effects on n-cdSe([KFe(CN)$_6$]3-2-) photoelectrochemistry”, **Solar Energy**. 52(2): 197–204; February, 1994.

[53] Nathan S. Lewis. “Toward Cost-Effective Solar Energy Use”, **American Association for the Advancement of Science**. 315: 798-801; Febuary, 2007.

[54] Khalil Ebrahim Jasim. “Dye Sensitized Solar Cells - Working Principles, Challenges and Opportunities”, **Solar Cells - Dye-Sensitized Devices**. 171-204; November, 2011.

[55] Monishka Rita Narayan. “Review: Dye sensitized solar cells based on natural photosensitizers”, **Renewable and Sustainable Energy Reviews**. 16(1): 208– 215; January, 2012.

[56] M. Gratzel. “Dye-sensitized solar cells”, **Journal of Photochemistry and Photobiology C: Photochemistry Reviews.** 4: 145-153; October, 2003.

[57] M. Späth and et al. “Reproducible manufacturing of dye-sensitized solar cells on a semi-automated baseline”, **PROGRESS IN PHOTOVOLTAICS: RESEARCH AND APPLICATIONS**. 11:207–220; 2003.

[58] J.-J. Lagref and et al. “Artificial photosynthesis based on dye-sensitized nanocrystalline TiO_2 solar cells”, **INORGANICA CHIMICA ACTA**. 361: 735-745, 2008.

[59] Matt Law and et al. “Nanowire dyesensitized solar cells”, **Nature Materials**. 4: 455-459; May, 2005.

[60] H. Gleiter. “Nanocrystalline materials”, **Progress in Materials Science.** 33: 223-315; May, 2003.

[61] Henrik Lindström and et al. “A new method to make dye-sensitized nanocrystalline solar cells at room temperature”, **Journal of Photochemistry and Photobiology A: Chemistry.** 145: 107-112; November, 2001.

REFERENCES (CONTINUED)

[62] A. Karami. “Synthesis of TiO_2 Nano Powder by the Sol-Gel Method and Its Use as a Photocatalyst”, **Journal of the Iranian Chemical Society**. 7: 154-160; July, 2010.

[63] Kai Zhu and et al. “Effects of Annealing Temperature on the Charge-Collection and Light-Harvesting Properties of TiO_2 Nanotube-Based Dye-Sensitized Solar Cells”, **Journal of Physical Chemistry C**. 114: 13433–13441; July, 2010.

[64] Ki-Seok Kim and et al. “Photovoltaic Properties of Nano-particulate and Nanorod Array ZnO Electrodes for Dye-Sensitized Solar Cell”, **Bulletin-Korean Chemical Society.** 27: 295-298; February, 2006.

[65] J B Baxter and et al. “Synthesis and Characterization of ZnO Nanowires and Their Integration into Dye-Sensitized Solar Cells”, **Nanotechnology.** 17: 304-312; June, 2006.

[66] Min Guo and et al. “The Effect of Hydrothermal Growth Temperature on Preparation and Photoelectrochemical Performance of ZnO Nanorod Array Films”, **Journal of Solid State Chemistry**. 178: 3210-3215; October, 2005.

[67] Tiwari A and Snure M. “Synthesis and characterization of ZnO nano-plant-like electrodes”, **Journal of Nanoscience and Nanotechnology**. 8: 3981-3987; August, 2008.

[68] Nazeeruddin MK and et al. “Combined experimental and DFT-TDDFT computational study of photoelectrochemical cell ruthenium sensitizers”, **Journal of the American Chemical Society**. 127: 16835-16847; December, 2005.

[69] Ryuji Kawano and et al. “High performance dye-sensitized solar cells using ionicliquids as their electrolytes”, **Journal of Photochemistry and Photobiology A: Chemistry**. 164: 87-92; 2004.

[70] Man Gu Kang and et al. “A 4.2% efficient flexible dyesensitized TiO_2 solar cells using stainless steel substrate”, **Solar Energy Materials and Solar Cells.** 90: 574-581; March, 2006.

REFERENCES (CONTINUED)

[71] Peng Wang and et al. "Stable ⩾8% efficient nanocrystalline dye-sensitized solar cell based on an electrolyte of low volatility", **Applied Physics Letters.** 86: 1-3; February, 2005.

[72] Shang-Di Mo and W. Y. Ching. "Electronic and optical properties of three phases of titanium dioxide: Rutile, anatase, and brookite", **PHYSICAL REVIEW B**. 51(19): 13023-13032; 15 May, 1995.

[73] Tim Luttrell and et al. "Why is anatase a better photocatalyst than rutile? - Model studies on epitaxial TiO_2 films", **SCIENTIFIC REPORT**. 4(4043): 1-8; 10 February, 2014.

[74] S. Wantawee, R. Vongwatthaporn and U. Tipparach. "Fabrication and Characterization of Titania (TiO_2) Nanotube Dye-Sensitized Solar Cells by Anodization Method", **Integrated Ferroelectrics**. 165: 153-158; 22 October, 2015.

[75] Karla S. Brammer and et al. "Biomaterials and Biotechnology Schemes Utilizing TiO_2 Nanotube Arrays", **Biomaterials Science and Engineering.** 193-210; September, 2011.

[76] M.M.Momeni and et al. "Silver nanoparticles decorated titanium dioxide-tungsten trioxide nanotube films with enhanced visible light photo catalytic activity", **Ceramics International**. 43: 564-570; January, 2017.

[77] Xiaosong Zhou and et al. "Preparation of B, N-codoped nanotube arrays and their enhanced visible light photoelectrochemical performances", **Electrochemistry Communications.** 13: 121-124; February, 2011.

[78] Qingyao Wang and et al. "Solvothermal preparation of Fe-doped TiO_2 nanotube Arrays for enhancement in visible light induced photoelectrochemical performance", **Journal of Alloys and Compounds**. 690: 139-144; January, 2017.

[79] Dharmasena Peramunage and Stuart Licht. "cation and speciation effects on n-cdSe([KFe(CN)6]$^{3-2-}$) photoelectrochemistry ", **Solar Energy**. 52: 197-204; February, 1994.

REFERENCES (CONTINUED)

[80] Andrei A. Bunaciu, Elena Gabriela UdriŞ Tioiu and Hassan Y. Aboul-Enein. “X - RAY DIFFRACTION: Instrumentation and Applications”, **Critical Reviews in Analytical Chemistry**. 45(4): 289-299; 1 April, 2015.

[81] Ana Violeta Girao, Gianvito Caputo and Marta C. Ferro. “Application of Scanning Electron Microscopy-Energy Dispersive X-ray Spectroscopy (SEM-EDS)”, **Comprehensive Analytical Chemistry**. 75: 152-167; June, 2011.

[82] Uros Maver and et al. “Recent progressive use of atomic force microscopy in biomedical applications”, **TrAC Trends in Analytical Chemistry**. 80: 96-111; June, 2016.

[83] Safia A.Kazmi and et al. “Electrical and optical properties of graphene-TiO_2nanocomposite and its applications in dye sensitized solar cells (DSSC)”, **Journal of Alloys and Compounds**. 691: 659-665; 15 January, 2017.

[84] M.Alitabar and H.Yoozbashizadeh. “Effect of sodium carbonate as an additive on the morphology and photocatalytic activity of TiO_2 nanotubes”, **Materials Research Bulletin**. 95: 169-176; November, 2017.

[85] A.A. Yadav and E.U. Masumdar. “Preparation and characterization of indium doped $CdS_{0.2}Se_{0.8}$ thin films by spray pyrolysis”, **Materials Research Bulletin**. 45(10): 1455-1459; October, 2010.

[86] Mohamad Mohsen and Momeni Yousef Ghayeb. “Photoelectrochemical water splitting on chromium-doped titanium dioxide nanotube photoanodes prepared by single-step anodizing”, **Journal of Alloys and Compounds**. 637: 393-400; 15 July, 2015.

[87] Efrat Korin, Natalya Froumin and Smadar Cohen. “Surface Analysis of Nanocomplexes by X-ray Photoelectron Spectroscopy (XPS)”, **ACS Biomaterials Science and Engineering**. 3(6): 882-889; April, 2017.

[88] Peng Gu and et al. “Fabrication and characterization of dye-sensitized solar cells based on natural plants”, **Chemical Physics Letters**. 693: 16-22; February, 2018.

REFERENCES (CONTINUED)

[89] Tallapragada V.S.S.P Sashank, Bhavirisetti Manikanta and Aparna Pasula. “Fabrication and Experimental Investigation on Dye Sensitized Solar Cells Using Titanium Dioxide Nano Particles”, **Materials Today: Proceedings**. 4(2): 3918-3925, 2017.

[90] M.Z.H. Khan and et al. “Performance improvement of modified dye-sensitized solar cells”, **Renewable and Sustainable Energy Reviews**. 71: 602-617; May, 2017.

[91] Sanjivani V.Umale and et al. “Fabrication, characterization and comparison of DSSC using anatase TiO_2 synthesized by various methods”, **Advanced Powder Technology**. 28(11): 2859-2864; November, 2017.

[92] Y. Marsumi1 and A.W. Pramono. “Influence of Niobium or Molybdenum in Titanium Alloy for Permanent Implant Application”, **Advanced Materials Research**. 900: 53–63; February, 2014.

[93] Gopal K.Mor and et al. “A review on highly ordered, vertically oriented TiO_2 nanotube arrays: Fabrication, material properties, and solar energy applications”, **Solar Energy Materials and Solar Cells**. 90(14): 2011–2075; 6 September, 2006.

[94] Mir Ghasem Hosseini, Mohamad Mohsen and Momeni Masoud Faraji. “Fabrication of Au-Nanoparticle/TiO_2-Nanotubes Electrodes Using Electrochemical Methods and Their Application for Electrocatalytic Oxidation of Hydroquinone”, **Electroanalysis**. 23: 1654-1662; May, 2011.

[95] Qingyao Wang. “Solvothermal preparation of Fe-doped TiO_2 nanotube arrays for enhancement in visible light induced photoelectrochemical performance”, **Journal of Alloys and Compounds.** 690: 139-144; January, 2017.

[96] Gopal K.Mor and et al. “A review on highly ordered, vertically oriented TiO_2 nanotube arrays: Fabrication, material properties, and solar energy applications”, **Solar Energy Materials and Solar Cells.** 90: 2011-2075; September, 2006.

REFERENCES (CONTINUED)

[97] M.Alitabar and H.Yoozbashizadeh. “Effect of sodium carbonate as an additive on the morphology and photocatalytic activity of TiO_2 nanotubes”, **Materials Research Bulletin**. 95: 169-176; November, 2017.

[98] Safia A.Kazmi and et al. “Electrical and optical properties of graphene-TiO_2nanocomposite and its applications in dye sensitized solar cells (DSSC)”, **Journal of Alloys and Compounds**. 691: 659-665; 15 January, 2017.

[99] M.Alitabar and H.Yoozbashizadeh. “Effect of sodium carbonate as an additive on the morphology and photocatalytic activity of TiO_2 nanotubes”, **Materials Research Bulletin**. 95: 169-176; November, 2017.

[100] A.A. Yadav and E.U. Masumdar. “Preparation and characterization of indium doped $CdS_{0.2}Se_{0.8}$ thin films by spray pyrolysis”, **Materials Research Bulletin**. 45(10): 1455-1459; October, 2010.

[101] Mohamad Mohsen and MomeniYousefGhayeb. “Photoelectrochemical water splitting on chromium-doped titanium dioxide nanotube photoanodes prepared by single-step anodizing”, **Journal of Alloys and Compounds**. 637: 393-400; 15 July, 2015.

[102] Mahmoud Zolfaghari and Mahshid Chireh. “Effect of Mn Dopant on Lattice Parameters and Band Gap Energy of Semiconductor ZnO Nanoparticles”, **Advanced Materials Research**. 829: 784-789; March, 2019.

[103] S. Khajoei Gharaei, M. Abbasnejad and Ryo Maezono. “Bandgap reduction of photocatalytic TiO_2 nanotube by Cu doping”, **Scienctific Report**. 8: 1-10; September, 2018.

[104] U. Tipparach and et al. "Preparation and characterization of nano-TiO_2 thin films by sol-gel dip-coating method”, **Nanotechnology**. 7: 129-136; June, 2008.

[105] Singh and et al. "Size and shape effects on the band gap of semiconductor compound nanomaterials" **Journal of Taibah University for Science**. 12(4): 470-475; May, 2018.

[106] K. Carneiro and et al. “Roughness Parameters of Surfaces by Atomic Force Microscopy”, **CIRP Annals**. 44(1): 517-522, 1995.

REFERENCES (CONTINUED)

[107] Dingding Tang and et al. "Effect of the composition of Ti alloy on the photocatalytic activities of Ti-based oxide nanotube arrays prepared by anodic oxidation", **Applied Surface Science**. 319: 181-188; 15 November, 2014.

[108] G. Hopfengärtner and et al. "XPS studies of oxidic model catalysts: Internal standards and oxidation numbers", **Journal of Electron Spectroscopy and Related Phenomena**. 63(2): 91-116; 2 August, 1993.

[109] L. Gomathi Devi and R. Kavitha. "A review on nonmetal ion doped titania for the photocatalytic degradation of organic pollutants under UV/solar light: Role of photogenerated charge carrier dynamics in enhancing the activity", **Applied Catalysis B: Environmental**. 140–141: 559-587; August-September, 2013.

[110] V. C. Anitha and et al. "Nonstoichiometry - Induced Enhancement of Electrochemical Capacitance in Anodic TiO_2 Nanotubes with Controlled Pore Diameter", **Journal of Physical Chemistry C**. 120(18): 9569–9580; 25 April, 2016.

[111] L. K. Preethi1 and et al. "A Study on Doped Heterojunctions in TiO_2 Nanotubes: An Efficient Photocatalyst for Solar Water Splitting", **Science Report**. 7: 14314; 30 October, 2017.

[112] C. Hinnen and et al. "An in situ XPS study of sputter-deposited aluminium thin films on graphite", **Applied Surface Science**. 78(3): 219-223; July, 1994.

[113] M. Alitabar and H. Yoozbashizadeh. "Improving the visible light photoelectron-chemical activity of synthesized TiO_2 nanotube arrays in an organic electrolyte containing sodium carbonate with doping by copper via single-step anodization", **New Journal of Chemistry**. 41: 10723–10730, 2017.

APPENDIX

PUBLICATIONS/PROCEEDING

PUBLICATIONS

1. **T.Thumsa-ard**, R.Laopaiboon and J.Laopaiboon. “Performance of Cu_2O doped recycled window glass as a thermoluminescence dosimeter”, Journal of Luminescence. 181: 286-290; January, 2017.
2. **T. Thumsa-ard**, R. Laopaiboon and J. Laopaiboon. “Performance of ZnO-doped recycled window glass as a thermoluminescence dosimeter ”, Journal of Physics: Confonference Series. 901(1): 1-5 ; September,2017.
3. R. Laopaiboon, **T.Thumsa-ard and** C.Bootjomchai.“The thermoluminescence properties and determination of trapping parameters of soda lime glass doped with erbium oxide”, Journal of Luminescence. 197: 304-309; May, 2018.
4. **Thanaporn Thumsa-ard**, Udom Tipparach, Narongsak Kodtharin, Orathai Thumthan. “Highly Ordered Titania Nanotube Arrays Synthesized via One-faced and Single-step Anodization”, Journal of Materials Science and Applied Energy. 8(1):379 – 388; April, 2019.

PROCEEDING

1. **T. Thumsa-ard**, R. Laopaiboon and J. Laopaiboon. “The role of Cu_2O dopant on the kinetic trapping parameters of thermoluminescence Thai commercial window glass”, Proceeding of 4th International Scientific Conference on Engineering and Applied Sciences**,** ISCEAS 2016: Organized by Beijing, Chaina, Pages 209-219.

VITAE

NAME	Miss Thnaporn Thumsa-ard
EDUCATION	2014 Bachelor Degree (Physics) Ubon Ratchathani University
	2016 Master Degree (Physics) Ubon Ratchathani University
SCHORLARSHIP	Science Achievement Scholarship of Thailand (SAST)
PUBLICATIONS	4 papers
	1 proceeding in international conference